TU Delft

# Array Processing in Atrial Fibrillation

## Application of different signal models and LAT estimation techniques

**MSc Thesis**

By Koen Rodewijk

# Array Processing in Atrial Fibrillation

## Application of different signal models and LAT estimation techniques

by

Koen Rodewijk

to obtain the degree of Master of Science
at the Delft University of Technology,
to be defended publicly on Thursday March 30, 2023 at 14:00.

Student number: 4453638
Project duration: May 22, 2022 – March 30, 2023
Thesis committee: Dr. ir. R. C. Hendriks, TU Delft, supervisor
Dr. ir. C. Varon, TU Delft
Dr. M. Mastrangeli, TU Delft

An electronic version of this thesis is available at http://repository.tudelft.nl/.

TU Delft

# Abstract

Atrial fibrillation (AF) is the most commonly occurring arrhythmia in clinical practice and can have a significant impact on the current and future wellbeing of the patient. By placing an unipolar sensor array directly on the epicardium during an open-heart surgery to measure the electrical activity of the atrium, more insight about this disease can be obtained. One method to obtain these insights is by applying common signal processing models to the measured electrogram (EGM). This thesis further investigates this application and argues why the most common array processing signal models are fundamentally incompatible with this application and proposes two different signal models to rectify the identified discrepancies. The proposed signal models are subsequently analyzed and the conclusion is drawn that both novel signal models better fit the EGM signals, but one signal model in particular shows promising results. This potential is exemplified by using this signal model to formulate a novel LAT estimation technique that can compete with state of the art LAT estimation methods in terms of estimation accuracy and execution time. This result shows the potential of the proposed signal model and opens the door to explore more applications in the future.

# Preface

This thesis concludes seven and a half years of studying Electrical Engineering at the Delft University of Technology for me. During this time I have learned countless things, both inside and outside my curriculum. From my study, I will mostly take away the mathematical and physical concepts that were taught to me and gave me the world view I have today. By just trying to rationally describe the things we see, we can ultimately explain it. I think this way of thinking is hugely valuable and is applicable to much more than Electrical Engineering alone.

This view also comes forward in this thesis. I started my thesis project by just describing what happens if the current theory around signal models is applied to cardiac impulses. From this one act, discrepancies quickly were noticed, and the work you have before you was born. I am happy with the thesis I can present to you today and if my thesis can successfully teach the reader (a fraction of) the matter it taught me during its process, I consider this report a success.

This thesis is not just a product of myself and the curriculum I have learned from the university. I also have other people to thank for the position I am in today. First and foremost, I have to thank my daily supervisor Richard for actively giving feedback, asking relevant questions, engaging in (lengthy) discussions, and in general being very accessible and easy to work with.

Furthermore, I want to thank my mother Rianne and sister Roos for giving me the foundation and opportunities that are vital for obtaining this degree. The fact that you have always supported and encouraged me means a lot and I owe you everlasting gratitude for it!

Finally, I would like to thank my friends for giving me much needed distractions and being a place were I can share the frustrations inherent to the “thesis life”. Special thanks hereby go out to Stijn and Tijs, who were willing to proof-read this report, and supply me with great feedback. Thank you guys!

*Koen Rodewijk*
*Delft, March 2023*

# Abbreviations

**AA** Atrial activity.

**AF** Atrial fibrillation.

**AP** Action potential.

**AV** Atrioventricular.

**ECG** Electrocardiography.

**EGM** Electrogram.

**ESPRIT** Estimation of signal parameters via rotational invariance techniques.

**EVD** Eigenvalue decomposition.

**FFT** Fast-Fourier transform.

**ICA** Independent component analysis.

**LAT** Local activation time.

**MSE** Mean square error.

**NCC-2** Time-domain cross-correlation method over second-order neighbours.

**NSR** Normal sinus rhythm.

**SA** Sinoatrial.

**SD** Steepest deflection.

**SNR** Signal-to-noise ratio.

**SPS** Signal Processing Systems department of TU Delft.

**SVD** Singular value decomposition.

**ULA** Uniform linear array.

**VA** Ventricular activity.

# Contents

# 1

# Introduction

According to the World Health Organization (WHO) cardiovascular diseases are the leading cause of death globally, representing 32% of all deaths worldwide [1]. As the life expectancy increases, the amount of patients suffering from these diseases is only expected to increase in the future [2], [3].

Although the list of cardiovascular diseases is vast, this thesis focuses on the most commonly occuring arrhythmia in clinical practice: atrial fibrillation (AF) [4]–[6]. Atrial fibrillation is a cardiac condition during which the atrial cells in the heart no longer fire synchronous to the centralized cardiac pacemaker: the sinoatrial node [7]. This causes an irregular or abnormal heart rate, which can have a significant impact on the current and future wellbeing of the patient. According to a study in Rotterdam approximately 24% of people older than 50 years are expected to obtain AF, which is shown to have a 1.5 to 1.9-fold mortality risk [3], [5]. These numbers depict the enormous benefits that can be gained by better understanding the mechanisms and treatments of AF.

Although the issue of AF is extensively looked at from a medical perspective, the Signal Processing Systems (SPS) department from the TU Delft, and by extension this thesis, approaches the problem from a different perspective: a signal processing perspective. Applying signal processing models to AF is not new, as will be discussed in the literature review of Chapter 2, but little research is performed on the precise consequences of applying standard signal processing models to this application. This thesis is therefore first concerned with obtaining a better theoretical understanding of applying general signal models to cardiac measurements. This topic is discussed in Chapter 3. In this chapter, three different signal models are compared and extensively looked at, from which one shows especially promising theoretical results.

This signal model is subsequently used in Chapter 4 in an estimation problem in which the activation times of the cardiac cells are obtained. The estimated values of the novel estimation techniques are compared to state of the art estimation techniques and a conclusion is drawn about the practical feasibilities of the novel techniques and signal models.

# 2

# Background

This background section aims to summarize the current state of affairs around the important subjects of atrial fibrillation and the connection with signal processing. The content described in this chapter will form the foundation of the identified research questions and how the subsequent research of this thesis is shaped.

This background first discusses the anatomy and normal operation of the heart in Section 2.1. Then the atrial fibrillation condition will be discussed in more detail in Section 2.2. Subsequently, the connection between atrial fibrillation and signal processing will be explored in Section 2.3. The chapter will end with a description surrounding the field of array processing in particular in Section 2.4.

## 2.1. Functioning of the heart in normal conditions

The heart is responsible for pumping blood through the body. It does this using its four chambers: two atria and two ventricles, one of each on the left and right side of the heart as depicted in Figure 2.1 [8]. The atria hereby act as a receiving chamber to push blood into the ventricles, which are responsible for the final “push” of the blood into the pulmonary or systemic circuits of the body [8]. This contraction of the cardiac muscle cells is controlled by an electric impulse that propagates through the tissue, which is initiated in the sinoatrial (SA) node. This principle is more precisely elaborated upon below.

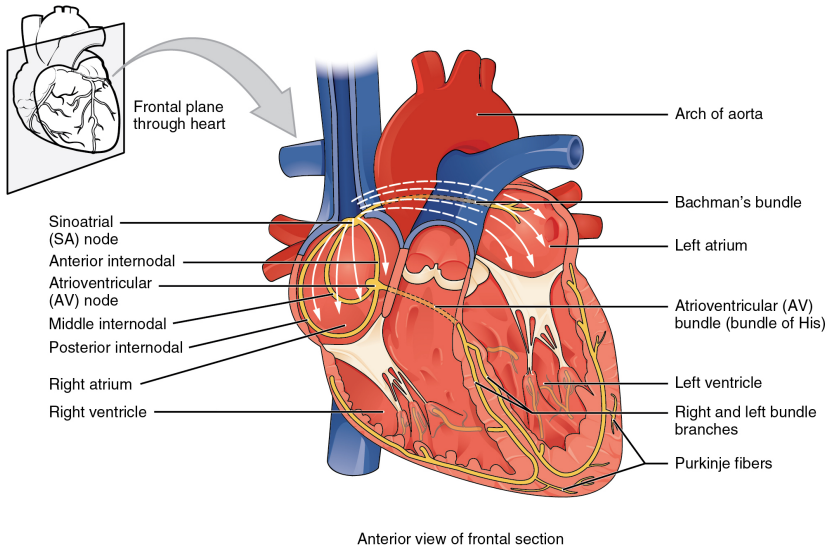


Figure 2.1: The anatomy and conduction system of the heart. Source: [8]

### 2.1.1. Electrical conduction through the heart

Individual cardiac muscle cells have the ability to autonomously initiate a periodic electrical impulse that causes the cell to contract. When multiple cardiac muscle cells are connected, they all follow the cell with the highest inherent impulse rate. The impulse subsequently travels from the faster to the slower cells in the tissue to trigger a contraction [8].

The electrical impulses propagate through the cardiac muscle tissue as a membrane potential that is caused by ion concentration differences between the intra- and extracellular environments. This membrane potential impulse is called an action potential (AP). An action potential shape is independent of the stimulus, and is induced when the membrane voltage reaches the threshold voltage of the cell in which case the cell "fires", creating a self-sustaining AP. Ion channels on the cell membrane selectively allow the in and out flow of electrically charged ions, which influences the membrane voltage and ultimately allows an action potential to exist and propagate across the tissue [9]. Figure 2.2 depicts how such an action potential is created in cardiac muscle cells using the voltage-gated ion channels in the cell membrane.

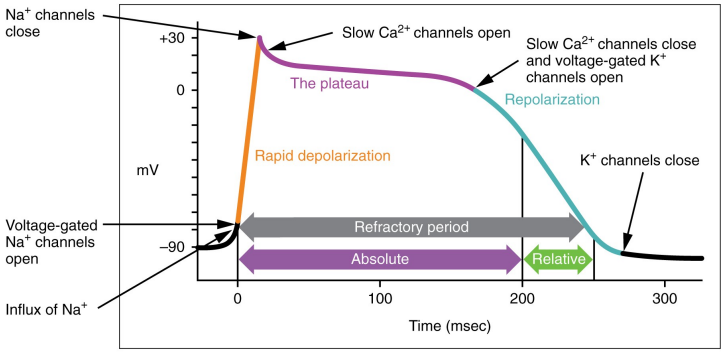


Figure 2.2: Creation of the action potential in cardiac contractile cells. Source: [8]

The two important phases of the AP are the depolarization and repolarization phases. The depolarization phase is characterized by a rapid increase in the membrane potential due to an inward current of positively charged ions into the cell. The repolarization phase subsequently equalizes the membrane voltage by allowing an outflux of positive ions. The time between the two phases is the refractory period. During this period the cell is not susceptible to a new stimulus to create another AP. This refractory period ensures the impulse cannot propagate backwards and that the muscles have time to relax [7]–[9].

As mentioned above, the fastest cell in the cardiac tissue determines the overall rate of the contraction. Within the heart this normal cardiac rhythm is established by the sinoatrial (SA) node. The SA node is a clump of tissue near the right atrium with the highest firing rate and is thus responsible for maintaining the normal sinus rhythm (NSR) of the heart [8].

Starting at the SA node, the electrical impulse propagates across both atria, guided by the atriaventricular septum, which prevents the AP from propagating into the ventricles. The only path towards the ventricles is via the atrioventricular (AV) node, which delays the signal by approximately 100 ms, before letting the signal through towards the atrioventricular bundle from where the impulse branches out through the ventricles [8]. This propapation path is also depicted in Figure 2.1.

### 2.1.2. AP propagation model

Accurate models for the generation and propagation of action potentials through atrial cells are of high value to cardiologists and AF research in general. Many of such models were therefore created, first based on animal cell measurements, which were later expanded to also include human atrial cell measurements [10]–[12]. Especially the model developed by Courtemanche *et al.* [12] still seems to be used extensively in research today. This model models the cell membrane voltage $V_m$ of a single cell as a capacitor with capacitance $C_m$ that is controlled by ionic and stimulus currents, $I_{ion}$ and $I_{st}$

respectively, as

$$\frac{\delta V_m}{\delta t} = \frac{-(I_{ion} + I_{st})}{C_m} \,. \tag{2.1}$$

Courtemanche *et al.* [12] subsequently give expressions for twelve different ionic currents that in total make up the ionic currents $I_{ion}$.

When modelling the propagation of the membrane potential over multiple cells, typically the diffusion of the membrane potential is added through the transmembrane current $I_{tm}$ that is governed by the Poisson-based, reaction-diffusion equation

$$I_{tm} = S_v^{-1} \nabla \cdot \mathbf{\Sigma} \nabla V_m \,, \tag{2.2}$$

where $S_v$ is the cellular surface-to-volume ratio, $\mathbf{\Sigma}$ contains the intracellular conductivities, and $V_m$ is the membrane potential [13], [14]. The $\nabla$-symbol is used as a divergence and gradient operator respectively. The complete AP propagation model over a two-dimensional tissue can then be expressed as

$$C_m \frac{\delta V_m}{\delta t} = I_{tm} + I_{st} - I_{ion} \,, \tag{2.3}$$

where $I_{tm}$ is the transmembrane current as described by Equation (2.2), $I_{st}$ is the stimulus current, and $I_{ion}$ is the total ionic current as described by the model of Courtemanche *et al.* [12], [13], [15].

## 2.2. Atrial fibrillation

Atrial fibrillation arises when the electrical conduction in the atria is disturbed, in which case atrial cells can fire asynchronously to the normal sinus rhythm. Although the immediate effects of AF do not have to be life-threatening, long-term AF can have serious adverse consequences [7].

The precise mechanisms that lie underneath AF are currently not yet fully understood and are of great interest to the medical community. According to the examined literature, three hypotheses currently exist that can explain AF. Any of these mechanisms, or a combination thereof, is expected to lie at the foundation of AF [7], [16], [17]. These hypotheses are:

1. **Ectopic foci:** Locations outside of the SA node exist that cause an undesired AP, as depicted in Figure 2.3A.
2. **Atrial remodeling**: Any change in atrial structure or function that can lead to atrial arrhythmia. Atrial remodeling can be caused by a multitude of conditions, under which also AF. This explains the progressive nature of the condition. Figures 2.3CD show two examples of atrial remodeling causing chaotic impulse propagation in atrial tissue.
3. **Re-entry circuits:** Specifically conditioned cardiac tissue that results in a self-maintained circulation of electrical impulses, as depicted in Figure 2.3B. This mechanism is a specific case of atrial remodeling and is sometimes also referred to as rotors.

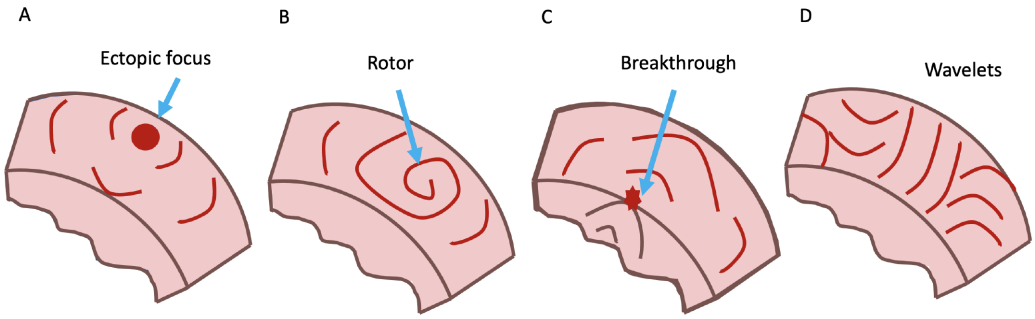


Figure 2.3: Four possible mechanisms that are expected to lie at the foundation of AF. C and D both correspond to the atrial remodeling hypothesis. Source: [18, p.14]

It is currently still unclear to what extent each of these individual mechanisms contribute to the overall AF condition of a patient. Which mechanism contributes the most can have a significant impact on which therapy is the most effective. For example, if a single ectopic foci is the cause of the arrythmia, the ablation of this malfunctioning tissue should be an effective treatment. However, if AF is the consequence of re-entry circuits, an effective treatment might be to divide the cardiac tissue into smaller, isolated zones instead [7]. It is also likely that the precise mechanisms of AF vary from person to person. Currently, arrhythmia mechanisms are generally not yet evaluated on an individual basis, but there exists a desire in the medical field to start assessing individual atrial structures and electrical properties to provide patient-specific treatment of AF [16], [17].

### 2.2.1. Treatments

As of 2018, two approaches for the treatment of AF exist: medicine-based and ablation-based. Both treatments are suboptimal and have a high reccurance rate (30% to 80% for medicine, and 40% to 60% for ablation) [16]. Until recently the ablation method was restricted to standardized ablation of certain tissue, but because of developments in mapping the electrical impulses in the heart it becomes increasingly possible to target patient-specific cardiac tissue for ablation, hereby also increasing the efficacy of the treatment [16], [19]–[21]. Although the first clinical application of these patient-specific ablation technologies have happened already, the technology is still in its infancy [16], [17]. The computations can take several days, and the imaging resolution is not high enough to properly identify faulty tissue with a high enough accuracy [16]. Improving these technologies therefore is one of the main research directions within AF.

## 2.3. Cardiac measurements and processing

The desire to increase the general understanding about AF attracts the interest of multiple academic fields, under which the signal processing community, due to the complicated mechanisms underlying AF. Signal processing is of particular interest to AF, because many important and desired cardiac tissue and impulse propagation properties are not easily observable. Sensor measurements therefore often require extensive processing before useful conclusions can be made. How to most accurately estimate these important parameters is an ongoing task within the biomedical signal processing field.

One of the most popular measurement techniques in use today is electrocardiography (ECG). ECGs are measurements taken from up to 12 electrodes placed on predetermined locations on the body, each measuring the electrical activity of the heart. A typical ECG first shows the depolarization of the atria in the P-wave, after which follows the de- and repolarization of the ventricles in the QRS-complex and T-wave respectively, as shown in Figure 2.4 [8]. A wide range of signal processing applications to this measurement technique exists. Some applications include but are not limited to the detection of the QRS-complex, noise elimination, atrial and ventricular source separation, and automatic arrhythmia classification [22]–[24].

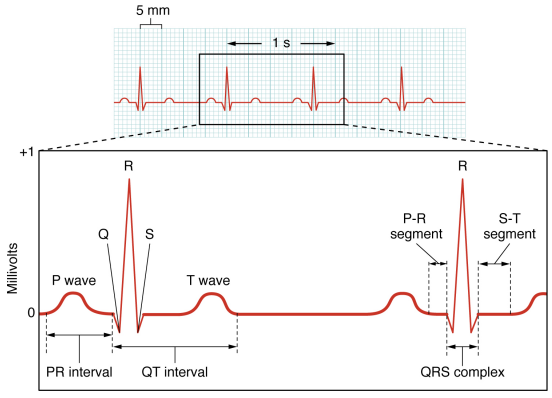


Figure 2.4: A typical ECG waveform. Source: [8]

### 2.3.1. Electrogram (EGM)

Although ECGs have proven to give useful information about AF, its information is still rather limited when compared to measuring atrial activity directly from the cardiac tissue using more invasive methods. Mapping atrial activity using catheter based sensing methods has been explored with mixed results [19], [25]–[27]. More recently, the Erasmus Medical Center has created a novel approach to obtain high resolution mapping of the electrical activity in the atria; using a 192 unipolar electrodes sensor array that is placed directly on the atrial epicardial tissue during an open-heart surgery [28]. This sensor array and an example electrogram (EGM) it generates is depicted in Figure 2.5. This thesis focuses on the usage of EGMs in particular in order to extract useful information about AF. Specifically the usage of a unipolar sensor array placed on the atrium is assumed throughout the rest of this thesis when referring to EGM measurements.

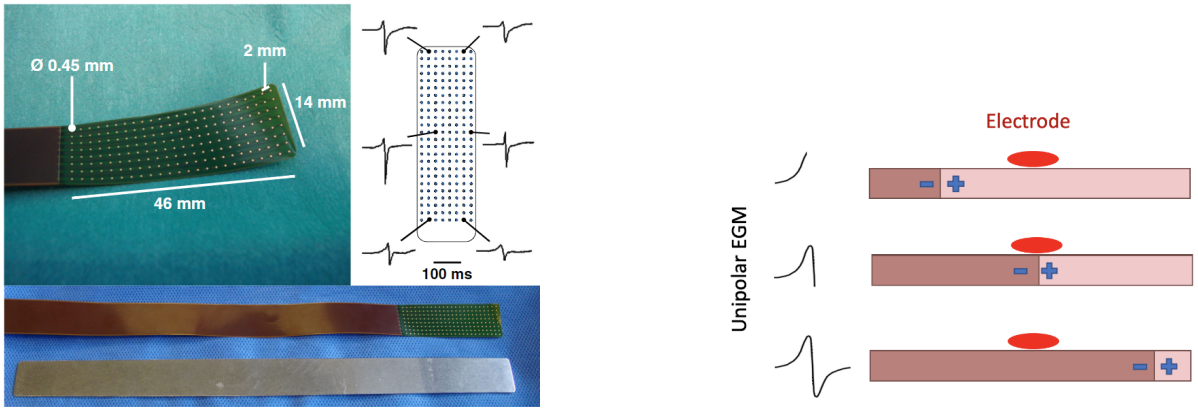


(a) (b)

Figure 2.5: (a) The used unipolar electrode array by the Erasmus Medical Center. Source: [28, p.222]. (b) Generated electrogram (EGM) signal from unipolar electrode when an impulse propagates underneath. Source: [18, p.12]

#### EGM model

An electrogram can be modelled by assuming it measures the sum of the electrical activity of the surrounding cells, weighted inversely with the distance between each cell and the electrode [13], [29]. When assuming a two-dimensional surface $A$ consisting of cardiac cells, the measured EGM voltage at location $\mathbf{y}$ can thus be modeled as

$$\phi(\mathbf{y}, t) = \frac{1}{4\pi\sigma_e} \iint_A \frac{I_{tm}(\mathbf{x}, t)}{\|\mathbf{y} - \mathbf{x}\|} d\mathbf{x} \,, \tag{2.4}$$

where $\sigma_e$ is a constant extracellular conductivity, and $I_{tm}(\mathbf{x}, t)$ is the transmembrane current at location $\mathbf{x}$ as described by Equation (2.2). This forward model can subsequently be used to formulate inverse problems to estimate important tissue parameters such as cell conductivities, anisotropy ratios, and activation times [13], [30], [31].

### 2.3.2. Local activation time (LAT) estimation

An accurate estimation of the local activation time (LAT) of the cells in atrial tissue is of great significance, because it can lead to the estimation of other tissue properties and can give an intuitive understanding about the impulse propagation through the tissue [31]–[33]. Typically, the activation time of a cell is defined as the moment when the cell depolarizes [33], [34]. An example of an activation map is depicted in Figure 2.6.

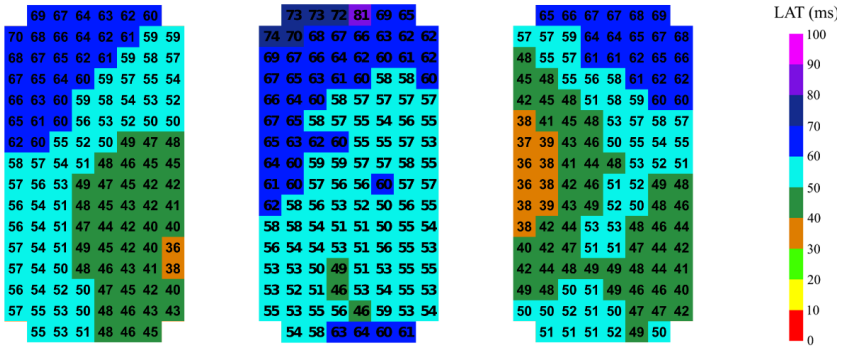


Figure 2.6: An example of an activation map of cardiac tissue. Source: [31, p.827]

Multiple LAT estimation techniques have been proposed in literature. One of the most commonly applied algorithms today is the Steepest Deflection (SD) method. This algorithm simply takes the minimum derivative of the EGM signal as the moment of activation [30], [34]. Given an EGM time series $\phi(t)$, the moment of activation $\tau$ is thus estimated as

$$\tau = \arg\min_{t} \frac{\delta\phi(t)}{\delta t} \ . \tag{2.5}$$

Although this method is easy to implement and produces reliable results in low noise conditions, the algorithm is quite sensitive to noise and (far-field) signal artifacts [32], [33]. Because of these problems, multiple suitable alternatives for the SD algorithms have been explored in literature. The literature review of Cantwell *et al.* [33] does an excellent job of enumerating these alternatives.

An SD algorithm alternative that shows especially promising results, is the algorithm proposed by Kölling *et al.* [32] using a time-domain cross-correlation method over higher-order neighbours. This algorithm first identifies neighbours to each sensor that are at most $P$ hops away and subsequently estimates the time delay of the AP between all defined neighbours. This time delay is estimated using the time domain cross-correlation between two neighbouring sensors $x_i(k)$ and $x_j(k)$, which is calculated as

$$\rho_{(i,j)}(s) = \sum_{k} \frac{(x_i(k) - \mu_i)\left(x_j(k-s) - \mu_j\right)}{\sqrt{\sigma_i^2 \sigma_j^2}} \ , \tag{2.6}$$

where $\mu_i$, $\mu_j$ are the means and $\sigma_i^2$, $\sigma_j^2$ are the variances of $x_i(k)$ and $x_j(k)$ respectively. The time delay between the two sensors $i$ and $j$ is then estimated as

$$\tau_{(i,j)} = \arg\max_{s} \rho_{(i,j)}(s) \ . \tag{2.7}$$

Lastly, Kölling *et al.* [32] use a least squares solution to transform the relative time delays between sensor-pairs to absolute time delays that are referenced to the same sensor.

In this thesis, this algorithm with only second order neighbours will be discussed, so $P = 2$, and this algorithm will be referred to as the NCC-2 algorithm in the continuation of this thesis.

## 2.4. Array signal processing and AF

Array signal processing is a subset of the signal processing field which focuses on signals conveyed by propagating waves that are measured by an array of sensors with distinct spatial locations [35], [36]. The ultimate goal of array processing is to extract as much information from these waves as possible using spatio-temporal processing techniques, also called beamforming [35]. Array processing has many applications, such as radio astronomy, radar imaging, audio processing, and telecommunication.

Within array processing a typical goal is to separate multiple statistically independent sources that are mixed in the measured signals [35]. This process is also referred to as source separation. Multiple existing source separation techniques are currently in existence.

These source separation techniques have also been applied to both ECG and EGM cardiac measurements, mostly to separate the measured atrial activity from the ventricular activity [22]–[24], [37]–[39]. The ventricular activity can namely obscure important information about the atrial activity.

An important assumption these array processing based implementations rely on is that the atrial and ventricular activity (AA & VA) are decoupled and are thus statistically independent processes. Although this assumption may not fully be correct from a physiological perspective (see section 2.1), array processing techniques have generally proven to increase the estimation of the atrial activity, especially when no arrhythmia are present [38], [39].

A description about a typical array processing model, how that model is used for source enumeration purposes, and how it has been used to separate AA from VA is described in the sections below.

### 2.4.1. General array processing signal model

Typically, array processing models assume $D$ spatially different source signals being transmitted over a linear medium to $M$ sensors placed in a specific spatial configuration [35], [36]. A typical sensor array geometry is the uniform linear array (ULA), which places $M$ identical sensors a constant distance $\Delta$ apart in a straight line. Figure 2.7 shows a depiction of such a model.

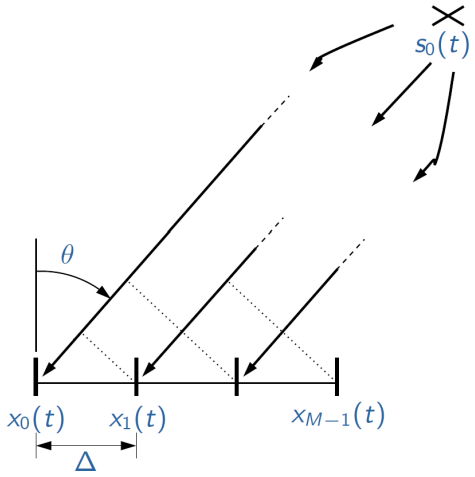


Figure 2.7: Typical far-field array processing model with $D = 1$ and ULA sensor configuration. Source: [40]

Each sensor thus measures a superposition of the individual transmitted sources up to a temporal convolution difference. Assuming each source $d$ is an independent stochastic process with realisation $s_d(t)$, with $h_{i,d}(t)$ the corresponding impulse response from source $d$ to the $i$th sensor, the measurements for the $i$th sensor $x_i(t)$ can be modelled as

$$x_i(t) = \sum_{d=0}^{D-1} h_{i,d}(t) * s_d(t) \ , \tag{2.8}$$

where $*$ denotes the convolution operator. Stacking all $M$ sensor measurements in a vector $\mathbf{x}(t) \in \mathbb{R}^{M\times 1}$ the model can thus be expressed as

$$\mathbf{x}(t) = \sum_{d=0}^{D-1} \mathbf{h}_d(t) * s_d(t) \ , \tag{2.9}$$

where $\mathbf{h}_d(t)$ is the vector stacking all impulse responses $h_{i,d}(t)$ from the $d$th source to the sensor array. Vector $\mathbf{h}_d$ can also be referred to as the steering vector or transfer function, because it "steers" the source signal $s_d(t)$ to each sensor; thereby taking into account all influences the propagation path has on the source signal (e.g. damping and time delay of the signal).

By assuming that the measurements can be split into time frames such that $s_d$ is stationary and ergodic across the time frames, Equation (2.9) can be transformed into the frequency domain and the convolution operation can be replaced by simple multiplication. The model for the measurement vector $\mathbf{x}(\omega) \in \mathbb{C}^{M\times 1}$ subsequently becomes

$$\mathbf{x}(\omega) = \sum_{d=0}^{D-1} \mathbf{h}_d(\omega) s_d(\omega) = \begin{bmatrix} \mathbf{h}_0(\omega) & \mathbf{h}_1(\omega) & \cdots & \mathbf{h}_{D-1}(\omega) \end{bmatrix} \begin{bmatrix} s_0(\omega) \\ s_1(\omega) \\ \vdots \\ s_{D-1}(\omega) \end{bmatrix} = \mathbf{H}(\omega)\mathbf{s}(\omega) \ , \tag{2.10}$$

where $\omega$ denotes the angular frequency. The elements $s_d(\omega)$ in the vector $\mathbf{s}(\omega)$ are assumed to be independent realisations of the corresponding complex-Gaussian, stationary stochastic process $S_d(\omega) \sim \mathcal{CN}(\mu_d(\omega), \sigma_d^2(\omega))$. In practice, any complex stochastic process can be assumed here, and this is merely chosen for simplicity purposes.

As a final addition to the model the measurement noise is added as independent realisations $\mathbf{n} \in \mathbb{C}^{M\times 1}$ of the identical zero-mean multivariate random variable $N \sim \mathcal{CN}(\mathbf{0}, \sigma_n^2\mathbf{I})$, where $\mathbf{0}$ is the $M$-dimensional zero vector, $\sigma_n^2$ the noise variance, and $\mathbf{I}$ the $M$-dimensional identity matrix. This leads to the final expression of a general array processing or ICA signal model

$$\mathbf{x}(\omega) = \mathbf{H}(\omega)\mathbf{s}(\omega) + \mathbf{n}(\omega) \ , \tag{2.11}$$

where $\mathbf{H}(\omega) \in \mathbb{C}^{M\times D}$ denotes the transfer matrix and $\mathbf{s}(\omega) \in \mathbb{C}^{D\times 1}$ the source signals at frequency $\omega$ [36], [41]. Also note that the noise realisations $\mathbf{n}(\omega)$ are assumed to be independent across frequencies $\omega$. Equation (2.11) will henceforth be referred to as the general signal model.

A typical beamforming problem is to construct a matrix $\mathbf{W}$ such that an estimation of the individual source signals $\hat{\mathbf{s}}(\omega)$ can be obtained from the measurement vector $\mathbf{x}(\omega)$ as [24], [36]

$$\hat{\mathbf{s}}(\omega) = \mathbf{W}\mathbf{x}(\omega). \tag{2.12}$$

### 2.4.2. Autocorrelation matrix and source enumeration of general signal model

Any spatio-temporal correlation between the sensor measurements can be investigated by the autocorrelation matrix $\mathbf{R}_x(\omega)$, which is calculated as

$$\mathbf{R}_x(\omega) = E[\mathbf{x}\mathbf{x}^H], \tag{2.13}$$

where $E[\cdot]$ denotes the expected value operator, and $^H$ denotes the Hermitian transpose. This autocorrelation matrix can be used to estimate the amount of sources $D$, as will be elaborated upon in this section. The process of estimating the number of sources is also referred to as source enumeration.

In order to obtain an intuitive expression for the autocorrelation matrix of the general signal model, the stochastic process $S_d(\omega)$ underlying the source signal realisations of Equation (2.11) is first separated into a deterministic variable $\mu_d(\omega)$, describing the expected value $E[S_d(\omega)] = \mu_d(\omega)$, and a new zero-mean stochastic process $\mathcal{E}_d(\omega) \sim \mathcal{CN}(0, \sigma_d^2(\omega))$ as

$$S_d(\omega) = \mu_d + \mathcal{E}_d, \tag{2.14}$$

where the dependence of both $\mu_d$ and $\mathcal{E}_d$ on the frequency $\omega$ is omitted for increased readability. This omission will also be done in future expressions in this thesis in the same manner.

Denoting the independent realisations of the process $\mathcal{E}_d(\omega)$ by $\varepsilon_d$, the signal model of Equation (2.11) can now be expressed without loss of generality as

$$\mathbf{x}(\omega) = \sum_{d=0}^{D-1} (\mu_d + \varepsilon_d)\mathbf{h}_d + \mathbf{n} \ , \tag{2.15}$$

where $\mu_d$ is the deterministic term of the $d$th source signal, $\varepsilon_d$ is the zero-mean stochastic component of the $d$th transmitted source signal, $\mathbf{h}_d$ is the steering vector corresponding to the $d$ts source, and $\mathbf{n}$ denotes the measurement noise.

When calculating the autocorrelation matrix of the general signal model defined above in Equation (2.15), it can be rewritten to group the deterministic and stochastic terms together to give

$$\mathbf{x}(\omega) = \underbrace{\left(\sum_{d=0}^{D-1} \mu_d \mathbf{h}_d\right)}_{\text{deterministic}} + \underbrace{\left(\sum_{d=0}^{D-1} \varepsilon_d \mathbf{h}_d\right)}_{\text{stochastic}} + \mathbf{n} = \mathbf{v} + \mathbf{w} + \mathbf{n} \ , \tag{2.16}$$

where $\mathbf{v}$ is the vector containing all deterministic terms from the model, and $\mathbf{w}$ is the vector containing the stochastic terms coming from the sources. The vector $\mathbf{n}$ still denotes the measurement noise.

Using Equation (2.16) and the observation that all stochastic variables are uncorrelated, the autocorrelation matrix $\mathbf{R}_x$ can subsequently be expressed as

$$\begin{aligned} \mathbf{R}_x(\omega) &= E[\mathbf{x}\mathbf{x}^H] = \mathbf{v}\mathbf{v}^H + E[\mathbf{w}\mathbf{w}^H] + E[\mathbf{n}\mathbf{n}^H] \\ &= \mathbf{v}\mathbf{v}^H + \sum_{d=0}^{D-1} \sigma_d^2 \mathbf{h}_d \mathbf{h}_d^H + \sigma_n^2 \mathbf{I} \ , \end{aligned} \tag{2.17}$$

where $\mathbf{v}$ is the deterministic component of Equation (2.16), $D$ is the number of sources, $\sigma_d^2$ is the variance of the $d$th source signal, $\mathbf{h}_d$ the transfer function corresponding to the $d$th source, $\sigma_n^2$ is the noise variance, and $\mathbf{I}$ denotes the identity matrix. The autocorrelation matrix can subsequently be split into

$$\mathbf{R}_x = \mathbf{R}_s + \mathbf{R}_n \ , \tag{2.18}$$

where $\mathbf{R}_s = \mathbf{v}\mathbf{v}^H + \sum_{d=0}^{D-1} \sigma_d^2 \mathbf{h}_d \mathbf{h}_d^H$ is the signal contribution to the matrix, and $\mathbf{R}_n = \sigma_n^2 \mathbf{I}$ is the noise contribution.

When only considering $\mathbf{R}_s$, a lower limit of the amount of sources $D$ can be estimated from the rank of the autocorrelation matrix $\mathbf{R}_s$. Namely, using the general property that for any matrix $\mathbf{A}$ and $\mathbf{B}$

$$\text{rank}(\mathbf{A} + \mathbf{B}) \leq \text{rank}(\mathbf{A}) + \text{rank}(\mathbf{B}) \ , \tag{2.19}$$

and that for any vector $\mathbf{g}$

$$\text{rank}(\mathbf{g}\mathbf{g}^H) = 1 \ , \tag{2.20}$$

the following conclusion about the rank of $\mathbf{R}_s$ can be obtained:

$$\text{rank}(\mathbf{R}_s) \leq 1 + D \ . \tag{2.21}$$

Or equivalently,

$$D \geq \text{rank}(\mathbf{R}_s) - 1 \ . \tag{2.22}$$

The relation that Equations (2.21) and (2.22) show, are believed to lie at the core of most source separation algorithms. Most literature namely assume that the rank of the autocorrelation $\mathbf{R}_x$ is related to the amount of sources present in the system [37]–[39].

How these expressions can be used to estimate the number of sources $D$ in the presence of noise is described in the next section.

### 2.4.3. Eigenvalue decomposition

Because of the noise term in Equation (2.17), $\mathbf{R}_x(\omega)$ will always be full rank. Therefore a method to differentiate the noise contribution from the signal contribution is required. This can done by using the eigenvalue decomposition (EVD) of $\mathbf{R}_x$.

Because $\mathbf{R}_s$ is Hermitian and positive semi-definite, the EVD of $\mathbf{R}_s$ can be written as

$$\mathbf{R}_s = \mathbf{U}\mathbf{\Lambda}\mathbf{U}^H \ , \tag{2.23}$$

with $\mathbf{U}$ being a unitary matrix whose columns are the eigenvectors of $\mathbf{R}_s$, and $\mathbf{\Lambda}$ is a diagonal matrix whose elements are the corresponding eigenvalues of $\mathbf{R}_s$. Because of Equation (2.21), $\mathbf{\Lambda}$ has at most $D+1$ nonzero diagonal elements.

Because the noise $\mathbf{n}$ is an independent, identically distributed (i.i.d.) process with autocorrelation matrix

$$\mathbf{R}_n = \sigma_n^2 \mathbf{I} = \sigma_n^2 \mathbf{U}\mathbf{U}^H \,, \tag{2.24}$$

$\mathbf{R}_x$ can be written as

$$\mathbf{R}_x = \mathbf{U}(\mathbf{\Lambda} + \sigma_n^2 \mathbf{I})\mathbf{U}^H \,, \tag{2.25}$$

which is the eigenvalue decomposition of $\mathbf{R}_x$. Note that the eigenvalue decomposition has $d+1$ "large" eigenvalues of size $\lambda_i + \sigma_n^2$, where $\lambda_i$ is a nonzero element of $\mathbf{\Lambda}$. The other "small" eigenvalues are of size $\sigma_n^2$. By detecting the amount of large eigenvalues of $\mathbf{R}_x$ the rank of $\mathbf{R}_s$, and thus the lower limit of sources $D$, can be estimated. In this thesis, this principle will be used in the same manner to estimate the rank of the $\mathbf{R}_s$ matrix, using the only available $\mathbf{R}_x$ matrix.

### 2.4.4. VA and AA separation in ECG and EGM signals

When considering the separation of the ventricular and atrial activity, most observed literature assume that the VA and AA are decoupled and they can directly apply the general signal model expressed by Equation (2.11) by defining two sources $D = 2$, one for the atrial activity and the other for the ventricular activity [22], [37], [39]. Using these assumptions, the implied model can subsequently be expressed as

$$\mathbf{x}(\omega) = \mathbf{h}_a(\omega) s_a(\omega) + \mathbf{h}_v(\omega) s_v(\omega) + \mathbf{n}(\omega) \,, \tag{2.26}$$

where $\mathbf{h}_a(\omega)$ and $s_a(\omega)$ are respectively the transfer function and source signal of the atrial activity, and $\mathbf{h}_v(\omega)$ and $s_v(\omega)$ are the transfer function and source signal of the ventricular activity. The vector $\mathbf{n}$ denotes the measurement noise.

The autocorrelation matrix of this model is therefore expressed as

$$\mathbf{R}_x(\omega) = \mathbf{v}\mathbf{v}^H + \sigma_a^2 \mathbf{h}_a \mathbf{h}_a^H + \sigma_v^2 \mathbf{h}_v \mathbf{h}_v^H + \sigma_n^2 \mathbf{I} \,, \tag{2.27}$$

where $\mathbf{v}$ denotes the expected value $E[\mathbf{x}(\omega)]$ of Equation (2.26), $\sigma_a^2$ and $\sigma_v^2$ denote the variance of the atrial and ventricular source signals respectively, $\mathbf{h}_a$ and $\mathbf{h}_v$ denote the transfer functions of the atrial and ventricular source signals respectively, $\sigma_n^2$ denotes the measurement noise variance, and $\mathbf{I}$ denotes the $M \times M$ identity matrix. The EVD of this autocorrelation matrix is expected to contain three large eigenvalues corresponding to the deterministic part $\mathbf{v}$ and the transfer functions $\mathbf{h}_a$ and $\mathbf{h}_v$, because they are all linearly independent from each other. This occurrence is believed to allow the subsequent ICA and source separation methods used in literature [39], [41]. Note that both transfer functions only add a large eigenvalue to $\mathbf{R}_x(\omega)$, because of their corresponding variances $\sigma_a^2$ and $\sigma_v^2$. Without these variances, $\mathbf{h}_a$ and $\mathbf{h}_v$ would become part of the deterministic part $\mathbf{v}$, which would make it impossible to distinguish the two sources from the EVD of the autocorrelation matrix.

As mentioned before, the application of this model on EGM and ECG measurements can successfully increase the estimation accuracy of the atrial parameters. However, when noise or arrhythmia are present, the performance can significantly drop again. This can have multiple reasons, such as statistical dependence between the VA and AA, misassumptions about the medium, or the presence of more than one atrial or ventricular component [39]. An interesting hypothesis hereby is that the atrial signal becomes too complex when arrhythmia are present to be accurately represented with a single source variable $s_a$, and multiple atrial sources thus are required. It would therefore be logical to extend the above signal model to $D$ atrial sources so that the model becomes

$$\mathbf{x}(\omega) = \sum_{d=0}^{D-1} \mathbf{h}_{a,d}(\omega) s_{a,d}(\omega) + \mathbf{h}_v(\omega) s_v(\omega) + \mathbf{n}(\omega) \,, \tag{2.28}$$

where $\mathbf{h}_{a,d}(\omega)$ and $s_{a,d}(\omega)$ now denote the transfer function and source signal of the $d$th atrial impulse source respectively. It can subsequently be hypothesized that this extended EGM signal model better reflects the EGM signals under AF conditions. This would also have significant effects when considering

the autocorrelation matrix of this extended model, because now the amount of large eigenvalues of the autocorrelation matrix is directly dependent on the amount of sources $D$ in the model, which is again dependent on AF. This theoretically should lead to a correlation between the presence of AF and the amount of large eigenvalues of the autocorrelation matrix, which could result in an effective feature to classify AF from EGM measurements.

However, as the next chapter will discuss, this extended EGM signal model actually is believed to be incompatible with cardiac electric impulses and this notion is therefore unfortunately not observable in practice. This idea will be further elaborated upon in the next chapter.

# 3

# Applying signal models to epicardial EGM signals during AF

Following the reasoning at the end of the previous chapter, a better understanding of applying the general signal model to AF EGM signals would be desirable. However, while obtaining this theoretical understanding, it becomes clear that the general signal model of the previous chapter is not capable of representing the atrial EGM signals with sufficient accuracy under AF conditions. Why the general signal model is theoretically incompatible with EGM signals is elaborated upon in Section 3.1.

In this chapter two novel signal models are therefore formulated with the goal to better fit the EGM signals during AF. These novel signal models are defined in Section 3.3. Thereafter, their application to EGM signals is first theoretically analyzed in Sections 3.4 and 3.5, before applying them to physiological simulations in Section 3.6. From the two performed analyses, one of the novel signal models eventually shows promising results in its ability to properly represent epicardial EGM measurements during AF. This signal model will subsequently be used in Chapter 4 to estimate the activation times of the cells underneath the sensors.

## 3.1. Problem formulation

The literature shows that the application of the general signal model to atrial, epicardial EGM measurements can be useful to separate the ventricular signal from the atrial signal when no arrhythmia are present. This leads to the observation that, when no arrhythmia are present, atrial signals can be accurately depicted using the single source signal $s_a$ in Equation (2.26). However, when arrhythmia are present, the general signal model of Equation (2.26) seems no longer able to accurately depict the electrical impulses in the atrium. Within the literature the hypothesis was made to increase the amount of atrial sources in the signal model to rectify this. However, this section will discuss why this extension theoretically is incorrect as well as why the application of the general signal model of Equation (2.11) to atrial electrical impulses in general is believed to be theoretically unsound and can therefore not be used as expected to extract information about AF from epicardial EGM signals, especially when arrhythmia are present.

### 3.1.1. Incompatibilities between general signal model and cardiac system

The general signal model of Equation (2.11) is not designed to model the propagation of action potentials in cardiac tissue, because their underlying mechanisms are fundamentally incompatible. When comparing the physiological mechanisms of electrical impulse propagation in cardiac tissue, as explained in Section 2.1, with the assumptions underlying the general signal model, as explained in Section 2.4.1, two key differences between the systems are namely identified. These two identified differences are discussed in the paragraphs Problems 1 and 2 below. After discussing these two fundamental problems in the underlying mechanisms, also a more practical problem of applying the general signal model to AF is identified, which will be explained below in problem 3.

**Problem 1 - Independent sources do not exist in cardiac tissue as they exist in the general signal model**
The general signal model assumes that the transmitted signals are directly measured up to a scalar multiplication in the frequency domain. Within cardiac tissue however, each cell creates its own action potential causing each cell in cardiac tissue to be regarded as its own source. This has significant effects on the application of the general signal model, because, when regarding the AP coming from a stimulation location of the tissue as the source, the independent variations of the source will be hidden from the measurements, causing the measured variation in the cardiac EGM signals to be indistinguishable from the independent measurement noise contribution.

This leads to the second term of the autocorrelation matrix expressed in Equation (2.17), $\sum_{d=0}^{D-1} \sigma_d^2 \mathbf{h}_d \mathbf{h}_d^H$, to disappear. This subsequently removes the dependence of the autocorrelation matrix on the amount of sources $D$, removing all correlation between the amount of sources and the rank of the autocorrelation matrix (without noise). This dependence is believed to be crucial when applying the general signal model to any ICA or (blind) source separation problems, as mentioned in Section 2.4.4. This also leads to the conclusion that simply adding more atrial source signals, as hypothesized in Section 2.4.4, is futile, because the rank of the autocorrelation matrix will not be influenced.

**Problem 2 - Non-linear behaviour of the system**
Another difference between the general signal model of Equation (2.11) and cardiac tissue is the non-linear behaviour of the cardiac system. When two wavefronts meet in the general system model, they superpose. Within cardiac tissue however, this superposition is impossible due to the inherent physiology of action potentials, and two meeting wavefronts in cardiac tissue will cancel each other out.

Although this difference also has significant effects on the application of the general signal model to cardiac impulses, the consequences are believed to not be as far reaching as for the first identified problem. As will be discussed in Section 3.3.1, this difference can actually be incorporated in the general signal model without much difficulty and far reaching consequences.

Also the refractory period in cardiac cells inhibits a non-linear factor, because it enforces a bound on the firing frequency of each cell. This difference is however not believed to be influential in this particular application, because this property can simply be incorporated in the transmitted source signals.

**Problem 3 - Non-stationary behaviour of cardiac signals**
The last identified problem is the reliance of the general signal model on the stationary behaviour of the source signals. The autocorrelation matrix of the general signal model that is expressed in Equation (2.17) in practice namely needs to be estimated over $K_w$ time frames as

$$\hat{\mathbf{R}}_x(\omega) = \frac{1}{K_w} \sum_{i=0}^{K_w-1} \mathbf{x}(\omega, i)\mathbf{x}(\omega, i)^H \ , \tag{3.1}$$

where $\mathbf{x}(\omega, i)$ is the measurement vector of size $M$ for frequency bin $\omega$ and the $i$th time frame. Note that the above equation can only add a rank-1 contribution to $\hat{\mathbf{R}}_x(\omega)$ from each time frame. The measurements $\mathbf{x}(\omega, i)$ are therefore required to be stationary between the time frames in order to obtain the theoretical autocorrelation matrix of Equation (2.17) where the independent variations between the time frames increase the rank of $\hat{\mathbf{R}}_x(\omega)$. In practice this assumption is however very difficult to uphold, especially under AF environments, because heartbeats tend to be different from each other.

Therefore, when estimating the autocorrelation matrix using Equation (3.1), non-ideal effects will significantly influence the estimation process, especially when each time frame has a realisation of a non-stationary process, which will add a linearly independent eigenvector to the matrix $\hat{\mathbf{R}}_x(\omega)$ each time frame, regardless of the cardiac properties.

### 3.1.2. Research question
These three identified problems make the application of the general signal model of Equation (2.11) to fibrillating epicardial EGM measurements quite dubious. This chapter therefore explores if a suitable alternative for this signal model can be formulated that better fits epicardial EGM measurements during

AF and if the alternative can subsequently be used to classify AF using the EVD of their autocorrelation, or any suitable alternative, matrix.

## 3.2. Methodology

To find a better signal model, two models are formulated in this chapter. The first signal model being an extension of the general signal model discussed in Section 2.4.1 and is referred to as the cardiac signal model. The other signal model uses a different approach by expressing the entire measurement spectra to each other, and will be referred to as the spectral signal model. Both models will first be defined below, in Section 3.3. The signal models are subsequently analyzed under different environmental assumptions, with the goal to obtain features from the signal models that successfully differentiate the scenarios. Three different scenarios are hereby formulated, each scenario representing a different physiological cardiac tissue structure from which two are connected to AF. The analyzed scenarios are:

1. **Normal sinus rhythm (NSR):** Normal heart operation with a single stimulation location and homogeneous tissue.
2. **AF remodeling:** Non-homogeneous tissue properties are present resulting in atypical heart function.
3. **AF ectopic foci:** Ectopic foci are present on the cardiac tissue, resulting in more than one stimulation location. The tissue is again considered homogeneous.

For all scenarios, a cardiac tissue that consists of a two-dimensional array of connected cardiac cells is assumed.

The subsequent performed analysis is twofold: first a theoretical analysis is done that investigates the rank of matrices that are formulated from the models. This theoretical analysis is discussed in Sections 3.4 and 3.5. Thereafter, the theory is validated in Section 3.6 using a physiological simulation in which the EVD and SVD of the defined matrices are investigated under the three different scenarios.

## 3.3. Definition of cardiac and spectral signal model

In this section two models are defined with the goal to better fit atrial EGM signals to the actual mechanisms in cardiac tissue. The first model is a generalization of the general signal model of the previous chapter that incorporates the first two problems mentioned in Section 3.1. The other model uses a different approach by expressing the measured signal spectra, instead of the individual samples. The first defined model will be referred to as the cardiac system model, and the second model as the spectral signal model in the continuation of this thesis.

An important assumption that is hereby added for both signal models is that only the AP impulse of the cell directly underneath the sensor is modelled. Far-field effects and spatial averaging of AP's are thus not taken into account. Although this assumption is quite improper, it is believed that useful conclusions can still be obtained with this assumption, because, as will become clear later in this section, the AP signal shapes denoted by the variable $\mathbf{s}$ in the signal models could be replaced with an EGM signal impulse shape. Secondary effects of the spatial averaging, e.g. superposition of opposing wavefronts, are lost in this assumption however. In Section 3.6 the true consequences of this assumption will become more clear, because in this section the actual EGM signals are used in the analysis.

Both models are derived below.

### 3.3.1. Cardiac signal model

To be able to apply the identified differences between the general signal model of Equation (2.11) and cardiac electrical impulse propagation, the general signal model is modified. As mentioned before, this modified model is referred to as the cardiac system model and will be derived in this section from the general signal model. This means that the general signal model will be used as a starting point from which the two key identified differences (problems 1 and 2 in Section 3.1) will be integrated.

The third problem of the problem formulation of Section 3.1 unfortunately could not be incorporated in the general signal model without changing its core structure. Integrating problem 3 into a practical

signal model is left to the spectral signal model defined in the next section.

**Incorporating problem 1 - Each cell is its own source:**
In order to integrate the idea that in cardiac tissue every cell is its own source, a slight paradigm shift and generalization from the general model is required.

It is assumed that each sensor $i$ now measures its own independent realisation $s_i(\omega)$ of the same stochastic process $S(\omega)$ with mean $\mu(\omega)$ and variance $\sigma^2(\omega)$, instead of each sensor measuring the same realisation of the source signal (but convoluted). Here, $\mu(\omega)$ represents the shape of a non-delayed action potential propagating under the sensor, and $\sigma^2(\omega)$ the signal shape deviations each cell can have due to creating its own independent AP. Any random distribution with the mentioned mean and variance can be assumed on the stochastic variable $S(\omega)$.

We then stack the independent AP shape realisations of all $M$ sensors into the vector $\mathbf{s}(\omega) \in \mathbb{C}^{M\times 1}$ as

$$\mathbf{s}(\omega) = \begin{bmatrix} s_1(\omega) \\ s_2(\omega) \\ \vdots \\ s_M(\omega) \end{bmatrix} \tag{3.2}$$

and incorporate the sensor-specific delay of this shape in the steering vector

$$\mathbf{h}(\omega) = \begin{bmatrix} e^{j\omega\tau_1} \\ e^{j\omega\tau_2} \\ \vdots \\ e^{j\omega\tau_M} \end{bmatrix}, \tag{3.3}$$

where $\tau_i$ represents the delay from the non-delayed AP signal shape $\mu(\omega)$ to the $i$th sensor. Since the non-delayed AP signal shape is expected to occur at the stimulation location of the AP, the variable $\tau_i$ can also be regarded as the delay from the AP between the stimulation location and sensor $i$. Note that a damping variable in the steering vector is unnecessary, because each cell is expected to create its own AP.

Combining both expressions allows the cardiac system model to be expressed as

$$\mathbf{x}(\omega) = \mathbf{s}(\omega) \odot \mathbf{h}(\omega) , \tag{3.4}$$

where the $\odot$-operator denotes the element-wise (or Hadamard) vector product. Note that the element-wise multiplication is required, because the AP signal shape can not be factored out, due to the AP shape being independent realisations between the sensors. This essentially allows each sensor to be regarded as their own source.

By splitting the realisations $s_i(\omega)$ into its deterministic variable $\mu(\omega)$ and zero-mean stochastic variable $\varepsilon(\omega)$, the model can be rewritten as

$$\mathbf{x}(\omega) = (\mu\mathbf{1} + \boldsymbol{\varepsilon}) \odot \mathbf{h} = \mu\mathbf{h} + diag(\boldsymbol{\varepsilon})\mathbf{h} , \tag{3.5}$$

where $\mu$ can now be considered as the shared, non-delayed AP signal shape between the sensors, and $\boldsymbol{\varepsilon}$ is the sensor-dependent AP shape variation that is characterized as a realisation of the zero-mean multivariate complex random variable $\mathcal{E}(\omega) \sim \mathcal{F}(\mathbf{0}, \sigma(\omega)^2\mathbf{I})$, where $\mathcal{F}(\mathbf{0}, \sigma(\omega)^2\mathbf{I})$ is any $M$-dimensional distribution with mean $\mathbf{0}$ and covariance $\sigma(\omega)^2\mathbf{I}$. The measurement noise is omitted in this model.

**Incorporating problem 2 - No superposition in cardiac tissue**
The absence of superposition in the cardiac system is only noticed when multiple sources are present. Within the cardiac system this corresponds to having multiple stimulation locations on the tissue. When this is the case, the lack of superposition can be modelled by checking which AP wavefront reaches the sensor first, and only simulating that AP. So, when considering two stimulation locations, $a$ and $b$, on the tissue, the $i$th element of the steering vector $\mathbf{h}(\omega)$ can be chosen as

$$h_i(\omega) = \begin{cases} e^{j\omega\tau_{i,a}}, & \tau_{i,a} < \tau_{i,b} \\ e^{j\omega\tau_{i,b}}, & \tau_{i,b} < \tau_{i,a} \end{cases} , \tag{3.6}$$

where $\tau_{i,a}$, $\tau_{i,b}$ denote the time delay from the stimulation location $a$ and $b$ to the $i$th sensor respectively. Above expression can also be generalized to more than two stimulation locations by always choosing the smallest $\tau_i$.

This results in the completed cardiac system model as

$$\mathbf{x}(\omega) = \mu\mathbf{h} + diag(\boldsymbol{\varepsilon})\mathbf{h} \,, \tag{3.7}$$

where $\mu(\omega)$ denotes the shared, non-delayed AP signal shape, $\mathbf{h}(\omega)$ denotes the steering vector as expressed in Equation (3.6), and $\boldsymbol{\varepsilon}(\omega)$ denotes the AP shape variations between the sensors.

This model can intuitively be understood by considering $\mu(\omega)$ as a typical AP signal shape that is delayed by the steering vector $\mathbf{h}(\omega)$ to each sensor individually. Because each cell realizes an independent AP, this is incorporated in the zero-mean stochastic variable $\boldsymbol{\varepsilon}(\omega)$. Figure 3.1 depicts a graphical representation of this cardiac system model.

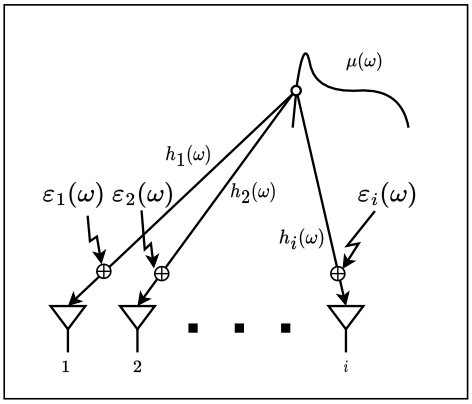


Figure 3.1: A visual representation of the cardiac system model.

### 3.3.2. Spectral model definition

The second defined signal model will consider the entire signal frequency spectrum measured in a time frame of sample size $F$. This differs significantly from the general and cardiac signal model, where each individual measurement sample was steered to each sensor. Instead of steering spatially different samples, this model explores what happens if entire spatially different spectra are steered to the sensors.

To investigate this, the measurement vector $\mathbf{x}_i$ now denotes an $F$-sized column vector representing the measured signal spectrum at sensor $i$. This vector $\mathbf{x}_i$ is modelled to consist of the uniformly scaled, time-delayed version of a reference AP signal spectrum $\mathbf{s} \in \mathbb{C}^F$, plus a sensor-dependent deviation vector $\boldsymbol{\varepsilon}_i \in \mathbb{C}^{F\times 1}$. The expression for the spectrum-based signal model thus becomes

$$\mathbf{x}_i = \mathbf{s} \odot \mathbf{h}_i + \boldsymbol{\varepsilon}_i = diag(\mathbf{s})\mathbf{h}_i + \boldsymbol{\varepsilon}_i \,, \tag{3.8}$$

where $\mathbf{s}$ denotes the reference non-delayed AP signal shape, $\mathbf{h}_i$ denotes the transfer function that delays the reference AP shape to the $i$th sensor, the $\odot$-operator denotes the element-wise vector product, and $\boldsymbol{\varepsilon}_i$ represents the sensor-specific deviations from the reference AP spectrum. Note that $\boldsymbol{\varepsilon}_i$ is not assumed to be a realisation of a zero-mean stochastic process in this model, as done in the cardiac signal model. The vector $\boldsymbol{\varepsilon}_i$ instead denotes all deviations from the purely time-delayed reference AP signal and is considered deterministic. Furthermore, this model also assumes that only one AP of the cell directly underneath the sensor is measured and no spatial averaging of AP's occurs.

Because the spectral signal model only models a delay of a reference AP signal, the transfer function

$\mathbf{h}_i$ of Equation (3.8) has the form

$$\mathbf{h}_i = \zeta_i \begin{bmatrix} 1 \\ e^{j2\pi\frac{1}{F}\tau_i} \\ e^{j2\pi\frac{2}{F}\tau_i} \\ \vdots \\ e^{j2\pi\frac{F-1}{F}\tau_i} \end{bmatrix} = \zeta_i \begin{bmatrix} 1 \\ \phi_i \\ \phi_i^2 \\ \vdots \\ \phi_i^{F-1} \end{bmatrix}, \quad \text{with } \phi_i = e^{j2\pi\frac{1}{F}\tau_i}, \tag{3.9}$$

where $\zeta_i$ is an attenuation factor that is uniform over the spectrum, $F$ is the sample size of the time frame, and $\tau_i$ is the delay between the reference AP signal $\mathbf{s}$ and the sensor $i$. Note that, when no time delay on the reference signal $\mathbf{s}$ is assumed, $\tau_i$ represents the moment of activation of the underlying tissue. A visual representation of the spectral signal model is given in Figure 3.2.

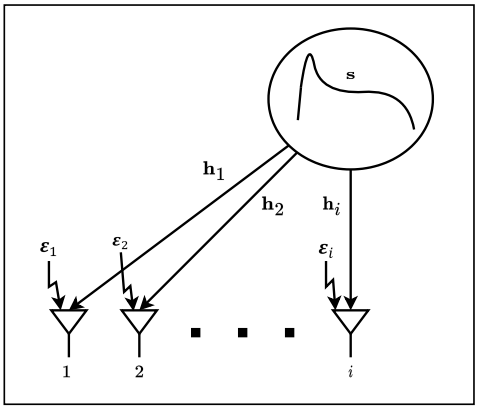


Figure 3.2: A visual representation of the spectral signal model.

The combination of Equations (3.8) and (3.9) is henceforth referred to as the spectral signal model. The application of this model to AF is analyzed further in Sections 3.5 and 3.6 of this chapter.

## 3.4. Theoretical analysis of cardiac signal model in AF environments

For each of the three mentioned scenarios in Section 3.2 an expression for the autocorrelation matrices $\mathbf{R}_x^{(1)}$, $\mathbf{R}_x^{(2)}$ and $\mathbf{R}_x^{(3)}$, and autocovariance matrices $\mathbf{C}_x^{(1)}$, $\mathbf{C}_x^{(2)}$ and $\mathbf{C}_x^{(3)}$ of the cardiac signal model described in Equation (3.7) is derived. These matrix expressions are subsequently used to conclude to what extend AF has an effect on the EVD of these matrices.

Each scenario relies on different mathematical assumptions regarding the homogeneity of the tissue and stimulation locations that are imposed on the cardiac signal model defined in section 3.3.1. These scenario-specific assumptions are integrated in the cardiac signal model to obtain a tailored expression for the measured signals. Using this new expression, the autocorrelation and autocovariance matrices are obtained for each scenario, which will subsequently be used to analyse the EVD of these matrices.

### 3.4.1. Normal sinus rhythm (NSR)

For the NSR scenario, a single stimulation location is assumed within a homogeneous tissue. This assumption essentially makes the cardiac signal model of Equation (3.7) directly applicable to this scenario. With $\mu(\omega)$ representing a non-delayed, shared AP signal shape, and $\boldsymbol{\varepsilon}(\omega)$ representing the independent AP variation between the sensors.

Therefore, the autocorrelation matrix $\mathbf{R}_x^{(1)}(\omega)$ of the signal model can be derived instantly from Equation

(3.7) as

$$\begin{aligned}\mathbf{R}_x^{(1)}(\omega) &= E[\mathbf{x}\mathbf{x}^H] = E[|\mu|^2\mathbf{h}\mathbf{h}^H + \mu\mathbf{h}\mathbf{h}^H(diag(\boldsymbol{\varepsilon}+\overline{\boldsymbol{\varepsilon}})) + diag(\boldsymbol{\varepsilon})\mathbf{h}\mathbf{h}^H diag(\overline{\boldsymbol{\varepsilon}})] \\ &= |\mu|^2\mathbf{h}\mathbf{h}^H + \sigma^2 diag\left(\mathbf{h}\odot\overline{\mathbf{h}}\right) ,\end{aligned} \tag{3.10}$$

where $\odot$ denotes the element-wise (or Hadamard) vector product and the bar denotes the complex conjugate operator.

The autocovariance matrix $\mathbf{C}_x^{(1)}$ is subsequently derived as

$$\mathbf{C}_x^{(1)} = \mathbf{R}_x - E[\mathbf{x}]E[\mathbf{x}]^H = \sigma^2 diag\left(\mathbf{h}\odot\overline{\mathbf{h}}\right) . \tag{3.11}$$

Exploiting the structure of $\mathbf{h}(\omega)$ given in Equation (3.6) by substituting it in Equation (3.11) allows the expressions to be simplified to

$$\mathbf{R}_x^{(1)}(\omega) = |\mu|^2\mathbf{h}\mathbf{h}^H + \sigma^2\mathbf{I} \tag{3.12}$$

and

$$\mathbf{C}_x^{(1)} = \sigma^2\mathbf{I} , \tag{3.13}$$

where $\mu(\omega)$ denotes the shared non-delayed AP impulse shape, $\mathbf{h}$ the steering vector as described in Equation (3.6), and $\sigma$ the variance of the zero-mean stochastic variable $\boldsymbol{\varepsilon}$.

**EVD of model in NSR scenario**
Analyzing Equations (3.13) and (3.12), it is clear that the shared signal shape term $|\mu|^2\mathbf{h}\mathbf{h}^H$ gives a rank-1 contribution to the autocorrelation matrix, which amounts to one large eigenvalue in $\mathbf{R}_x$. So, when no sensor-dependent deviations of the action potentials exist (so $\sigma = 0$), the autocorrelation matrix is simply expected to be rank-1.

The independent variations between the sensors therefore cause the rank of the autocorrelation and autocovariance matrix to increase to full-rank. This is depicted in the expected eigenvalue pattern as $M-1$ smaller eigenvalues of size $\sigma^2$. This eigenvalue pattern is comparable to the eigenvalue pattern of the autocorrelation matrix constructed from the general signal model with a single source with independent measurement noise that is expressed in Equation (2.17).

### 3.4.2. AF remodeling

To analyse the AF remodeling scenario, it is assumed that two disjoint tissue parts exist: part A and part B. The APs generated in each tissue part are by definition different from each other.

So, the signal shape realisations $s_i(\omega)$ of Equation (3.2) are now assumed to be independent realisations of random variable $S(i,\omega)$, which is now dependent on the sensor $i$ and consists of two different independent stochastic variables as

$$S_i(\omega) = \begin{cases} S_A \sim \mathcal{F}(\mu_a(\omega), \sigma_a(\omega)^2), & i \in A \\ S_B \sim \mathcal{F}(\mu_b(\omega), \sigma_b(\omega)^2), & i \in B \end{cases} , \tag{3.14}$$

where $\mathcal{F}(\mu,\sigma^2)$ is any random distribution with mean $\mu$ and variance $\sigma^2$, $i$ denotes the sensor, and $A$ and $B$ denote the disjoint sets of sensors in part A and B of the tissue respectively.

Incorporating the above changes in the model expressed by Equation (3.7) and separating the deterministic and stochastic terms of Equation (3.14) in the same manner as done in Equation (2.14), the cardiac signal model can now be written as

$$\mathbf{x}(\omega) = \mathbf{h}_a\mu_a + \mathbf{h}_b\mu_b + diag(\boldsymbol{\varepsilon}_a)\mathbf{h}_a + diag(\boldsymbol{\varepsilon}_b)\mathbf{h}_b , \tag{3.15}$$

where $\mu_{a,b}$ and $\boldsymbol{\varepsilon}_{a,b}$ depict the shared signal shape sample and variations respectively for tissue type A and B, and $\mathbf{h}_{a,b} \in \mathbb{C}^{M\times 1}$ depict the time delay to each sensor and are complementary to each other so that the $i$th element $h_{i,a/b}$ in $\mathbf{h}_a$ and $\mathbf{h}_b$ is

$$h_{i,a} = \begin{cases} e^{j\omega\tau_i}, & i \in A \\ 0, & \text{otherwise} \end{cases} \quad \text{and} \quad h_{i,b} = \begin{cases} e^{j\omega\tau_i}, & i \in B \\ 0, & \text{otherwise} \end{cases} , \tag{3.16}$$

where $\tau_i$ denotes the time delay of the non-delayed AP to the sensor $i$, and $A$ and $B$ are the disjoint sets denoting in which tissue each sensor is. The vectors $\mathbf{h}_a$ and $\mathbf{h}_b$ are thus of the same size, but the non-zero elements in $\mathbf{h}_a$ are zeroes in $\mathbf{h}_b$, and vice versa.

Using Equation (3.15), the autocorrelation matrix is subsequently derived as

$$\begin{aligned}\mathbf{R}_x^{(2)}(\omega) &= E[\mathbf{x}\mathbf{x}^H] = \mu_a^2\mathbf{h}_a\mathbf{h}_a^H + \mu_b^2\mathbf{h}_b\mathbf{h}_b^H + \sigma_a^2 diag(\mathbf{h}_a\mathbf{h}_a^H) + \sigma_b^2 diag(\mathbf{h}_b\mathbf{h}_b^H) + 2\mu_a\mu_b(\mathbf{h}_a\mathbf{h}_b^H + \overline{\mathbf{h}_a\mathbf{h}_b^H}) \\ &= \mathbf{v}\mathbf{v}^H + \sigma_a^2 diag(\mathbf{h}_a \odot \overline{\mathbf{h}_a}) + \sigma_b^2 diag(\mathbf{h}_b \odot \overline{\mathbf{h}_b}) \ ,\end{aligned} \tag{3.17}$$

where $\mathbf{v} = \mathbf{h}_a\mu_a + \mathbf{h}_b\mu_b$ is the deterministic part of the signal model of Equation (3.15). The autocovariance matrix of this model can now be derived as

$$\mathbf{C}_x^{(2)}(\omega) = \sigma_a^2 diag(\mathbf{h}_a \odot \overline{\mathbf{h}_a}) + \sigma_b^2 diag(\mathbf{h}_b \odot \overline{\mathbf{h}_b}) \ . \tag{3.18}$$

By exploiting the complementary structure between the $\mathbf{h}_a$ and $\mathbf{h}_b$ vectors described by Equation (3.16), the autocovariance matrix can more intuitively be expressed as

$$[\mathbf{C}_x^{(2)}]_{kl} = \begin{cases} \sigma_a^2 \ , & k = l \in A \\ \sigma_b^2 \ , & k = l \in B \\ 0 \ , & \text{otherwise} \end{cases} \ , \tag{3.19}$$

where $[\mathbf{C}_x^{(2)}]_{kl}$ denotes the element at the $k$th row and $l$th column of $\mathbf{C}_x^{(2)}(\omega)$, $A$ and $B$ denote the disjoint sets of tissue. Note that $\mathbf{C}_x^{(2)}(\omega)$ is a diagonal matrix.

**EVD of model in AF remodeling scenario**

Analyzing Equation (3.17) and (3.19), two interesting aspects are noticed. Firstly, the amount of large eigenvalues of the autocorrelation matrix of Equation (3.17) is still one; the single eigenvalue caused by the deterministic part $\mathbf{v}\mathbf{v}^H$ of $\mathbf{R}_x^{(2)}$. Secondly, the difference between the tissue parts only comes forward in the autocorrelation and autocovariance matrices through the difference in variances $\sigma_a^2$ and $\sigma_b^2$. The actual difference in signal shape does not have an influence on the eigenvalues of these matrices. Although, from Equation (3.19) it theoretically would still be possible to identify atypical cardiac tissue, if the atypical nature of the tissue results in a difference in AP shape variations.

The above result can also be generalized to more than two tissue parts: the amount of large eigenvalues of the autocorrelation matrix remains one, and only the difference in variances of the resulting AP signal shapes between the tissue parts has an influence on the eigenvalue pattern of the autocorrelation and autocovariance matrix.

### 3.4.3. AF ectopic foci

This scenario will investigate how multiple stimulation locations can be modeled using the cardiac system model of Equation (3.7).

When following the paradigm used for the reference signal model, we would like to be able to write the measurements $\mathbf{x}(\omega) \in \mathbb{C}^{\mathbb{M}\times\mathbb{1}}$ as the sum of the AP impulses coming from the $D$ different stimulation locations as

$$\mathbf{x}(\omega) = \sum_{d=0}^{D-1} (\mu\mathbf{h} + diag(\boldsymbol{\varepsilon})\mathbf{h})_d = \sum_{d=0}^{D-1} diag(\mu_d\mathbf{1} + \boldsymbol{\varepsilon}_d)\mathbf{h}_d \ , \tag{3.20}$$

where $\mu_d(\omega)$ is the $d$th AP stimulation source on the tissue, $\boldsymbol{\varepsilon}_d$ are the corresponding AP variations, and $\mathbf{h}_d(\omega)$ is the steering vector that delays the $d$th source from the stimulation location to the sensor accordingly.

However, as was already discussed at the end of section 3.1, different wavefronts do not superpose in cardiac tissue and each cell acts as its own source. The shape and variations of the measured AP signals thus do not change in this scenario when compared to the NSR scenario of Section 3.4.1. Therefore the expected signal shapes for each source are

$$\mu_0 = \mu_1 = \cdots = \mu_{D-1} = \mu$$

and the random variables underlying the realisations $\boldsymbol{\varepsilon}_d$ are also

$$\mathcal{E}_0 = \mathcal{E}_1 = \cdots = \mathcal{E}_{D-1} = \mathcal{E}$$

which allows the $\mu_d$ and $\boldsymbol{\varepsilon}_d$ of Equation (3.20) to be factored out. Therefore Equation (3.20) can now be rewritten as

$$\mathbf{x}(\omega) = \sum_{d=0}^{D-1} diag(\mu_d \mathbf{1} + \boldsymbol{\varepsilon}_d)\mathbf{h}_d = diag(\mu \mathbf{1} + \boldsymbol{\varepsilon})\left(\sum_{d=0}^{D-1} \mathbf{h}_d\right) = \mu\tilde{\mathbf{h}} + diag(\boldsymbol{\varepsilon})\tilde{\mathbf{h}}\,, \tag{3.21}$$

where $\tilde{\mathbf{h}} = \sum_{d=0}^{D-1} \mathbf{h}_d$, with each $\mathbf{h}_d$ being complementary to each other as expressed in Equation (3.6).

The autocorrelation matrix of this scenario can now be expressed as

$$\mathbf{R}_x^{(3)}(\omega) = |\mu|^2 \tilde{\mathbf{h}}\tilde{\mathbf{h}}^H + \sigma^2 \mathbf{I}\,, \tag{3.22}$$

where $\mu(\omega)$ is the shared AP signal shape sample between the sensors, $\tilde{\mathbf{h}}(\omega)$ is the summation of the complementary $\mathbf{h}(\omega)$-vectors corresponding to each stimulation location, as expressed above, and $\sigma^2(\omega)$ is the variance of the sensor-dependent realisations on the received AP signal shape.

The autocovariance matrix can lastly be derived as

$$\mathbf{C}_x^{(3)}(\omega) = \sigma^2 \mathbf{I}\,, \tag{3.23}$$

where $\sigma^2(\omega)$ is the variance of the sensor-dependent variations on the received signal shape.

**EVD of model in ectopic foci scenario**
Analyzing Equations (3.22) and (3.23), they look very similar to the matrices derived in the NSR scenario in section 3.4.1. The same eigenvalue pattern as in the NSR scenario is therefore expected in this scenario. Which means that one large eigenvalue is expected in the autocorrelation matrix $\mathbf{R}_x^{(3)}(\omega)$, and $\mathbf{C}_x^{(3)}$ consists of $M$ amount of equal eigenvalues of size $\sigma^2$.

### 3.4.4. Conclusion theoretical analysis of cardiac signal model

Summarizing the results of the obtained expressions of the autocorrelation and autocovariance matrices, the cardiac signal model might behave differently than expected from the ideas behind the general signal model. The autocorrelation matrices $\mathbf{R}_x^{(1)}$, $\mathbf{R}_x^{(2)}$ and $\mathbf{R}_x^{(3)}$ namely always have only one large eigenvalue, regardless of the amount of stimulation locations and non-homogeneous tissue properties. This is counter intuitive when following the general signal model paradigm in which the amount of large eigenvalues is correlated with the amount of sources. The number of large eigenvalues of both the autocorrelation and autocovariance matrices thus cannot give any useful information regarding AF from epicardial EGM measurements.

One interesting aspect that did come forward in the analysis is in the AF remodeling scenario. In that scenario the tissue properties do come forward in the eigenvalues of the matrices, which can provide useful information about the heart. However, because these eigenvalues are dependent on the variance of the signals and the third problem of Section 3.1 (non-stationary behaviour of cardiac system) is not remedied, the many practical problems to estimate this variance still exist. Within a single heartbeat, it is actually impossible to estimate this parameter at all.

This leads to the conclusion that the eigenvalue pattern of the autocorrelation matrix of the defined cardiac system model, in which the measurements are expressed per frequency bin $\omega$, does not incorporate much information about AF, especially when extracting information from data measured within a single heartbeat. When extending the measurements to multiple heartbeats, and finding a way to properly handle the non-stationary behaviour of the heart, it theoretically is possible to extract information about cardiac tissue properties from the eigenvalue pattern of the autocorrelation or autocovariance matrix.

This conclusion causes a desire for a signal model that can give useful expressions about impulse and/or tissue properties from measurements taken within a single heartbeat and is therefore not reliant on the measured variances of the signals. This desire led to the spectral signal model defined in Section 3.3.2. Its behaviour during the same three defined scenarios is analyzed in the next section.

## 3.5. Theoretical analysis of spectral signal model in AF environments

The same theoretical analysis as performed in the previous section for the cardiac signal model is now performed for the spectral signal model. This analysis is done for the same three scenarios that are defined in Section 3.2. A crucial difference however is that not the autocorrelation matrix $\mathbf{R}_x = E[\mathbf{x}\mathbf{x}^H]$ is hereby calculated, but a new matrix $\mathbf{B}$ is formulated on which the analysis is performed. This new matrix $\mathbf{B} \in \mathbb{C}^{F \times M}$ is formed by stacking the $M$ measured spectra $\mathbf{x}_i$ to give

$$\mathbf{B} = \begin{bmatrix} \mathbf{x}_1 & \mathbf{x}_2 & \cdots & \mathbf{x}_M \end{bmatrix} . \tag{3.24}$$

Furthermore, next to analyzing the rank of the matrix $\mathbf{B}$, also an analysis on the matrix

$$|\mathbf{B}| = \begin{bmatrix} |\mathbf{x}_1| & |\mathbf{x}_2| & \cdots & |\mathbf{x}_M| \end{bmatrix} \tag{3.25}$$

is performed, where $|\cdot|$ denotes an element-wise absolute value operator. This is done, because this removes the phase information from the model, resulting in a method to only analyze the morphology of the measured signals. This allows the $|\mathbf{B}|$ matrix to be a lower rank when no AF is present and the signal morphologies are similar. It is hypothesized that when AF is present, more variance in the signal morphologies between the sensors exists, resulting in a $|\mathbf{B}|$ matrix of a higher rank. This hypothesis is further explained in this section and tested in the physiological simulation performed in Section 3.6.

Just as in the previous section, each scenario will rely on different mathematical assumptions that are imposed on the spectral signal model. Expressions for the $\mathbf{B}$ and $|\mathbf{B}|$ matrices are subsequently derived and analyzed to show how the rank of these matrices are influenced under the different assumptions.

Unlike the cardiac signal model, the spectral signal model does not require the use of stochastic processes in the signal model definition in Section 3.3.2 and only deterministic variables are therefore used. This means that an analysis of the rank of the derived matrices is sufficient, instead of requiring an analysis of the singular value decomposition (SVD) of the matrices.

Lastly, in this analysis the assumption is also made that only one AP of the cell directly underneath the sensor is measured and no spatial averaging of APs occurs.

### 3.5.1. Normal sinus rhythm (NSR)

In this scenario, a single stimulation location again is assumed on a homogeneous tissue. Because the tissue is homogeneous it is therefore also assumed that all measured signal spectra are the same, up to a single time delay. This allows the removal of the $\boldsymbol{\varepsilon}_i$ term of Equation (3.8) so that the signal spectrum from sensor $i$ can simply be modelled as

$$\mathbf{x}_i = \mathbf{s} \odot \mathbf{h}_i = diag(\mathbf{s})\mathbf{h}_i , \tag{3.26}$$

where $\mathbf{s}$ is the non-delayed reference AP signal spectrum and $\mathbf{h}_i$ denotes the time delay of this AP signal to the $i$th sensor, as described in Equation (3.9).

The matrix $\mathbf{B}$ can now be expressed as

$$\mathbf{B} = \begin{bmatrix} \mathbf{x}_1 & \mathbf{x}_2 & \cdots & \mathbf{x}_M \end{bmatrix} = diag(\mathbf{s})\mathbf{H} , \tag{3.27}$$

where $\mathbf{s}$ is the reference AP signal and $\mathbf{H} = \begin{bmatrix} \mathbf{h}_1 & \mathbf{h}_2 & \cdots & \mathbf{h}_M \end{bmatrix}$ being the steering vectors responsible for the time delay.

Note that, because $diag(\mathbf{s})$ is full-rank and diagonal, the rank of the $\mathbf{B}$ matrix is directly dependent on the rank of $\mathbf{H}$. By definition, the rank of the matrix $\mathbf{H}$ is equal to the amount of linearly independent column vectors $\mathbf{h}_i$. Because the equation

$$\alpha\mathbf{h}_a + \beta\mathbf{h}_b = 0, \quad a \neq b, \quad a, b \in \{1, 2, \ldots, M\}, \quad \alpha, \beta \in \mathbb{R} \tag{3.28}$$

only has a solution when $\tau_a = \tau_b$, where $\tau_{a,b}$ denote the different time delays $\tau$ in Equation (3.9) corresponding to the different sensors. It is therefore concluded that the matrix $\mathbf{B}$ is full rank, unless no time delay between the measured spectra is present.

When considering only the magnitude of the measured vectors, the $|\mathbf{B}|$ matrix can be expressed as

$$|\mathbf{B}| = \begin{bmatrix} |\mathbf{x}_1| & |\mathbf{x}_2| & \cdots & |\mathbf{x}_M| \end{bmatrix} = diag(|\mathbf{s}|)|\mathbf{H}|. \tag{3.29}$$

From the expression above it becomes clear that the rank of $|\mathbf{B}|$ now is equal to the rank of $|\mathbf{H}| = [|\mathbf{h}_1| \quad |\mathbf{h}_2| \quad \cdots \quad |\mathbf{h}_M|]$. Because of the purely time-delay model assumption of Equation (3.9), the absolute value of each vector $|\mathbf{h}_i| = \zeta_i \, \mathbf{1}$, and the $|\mathbf{H}|$ matrix thus becomes

$$|\mathbf{H}| = \begin{bmatrix} \zeta_1 \mathbf{1} & \zeta_2 \mathbf{1} & \cdots & \zeta_M \mathbf{1} \end{bmatrix} , \tag{3.30}$$

where $\mathbf{1}$ denotes the all-ones column vector. Equation (3.30) clearly shows that $|\mathbf{H}|$ is a rank-1 matrix.

Therefore, it is concluded that the rank of the matrix $\mathbf{B}$ will always be full, unless the AP reaches two or more sensors at exactly the same time. Furthermore, when only measuring the magnitude spectrum of a purely time-delayed AP, the rank of the matrix $|\mathbf{B}|$ will always be one.

### 3.5.2. AF remodeling

Just as in Section 3.4.2, in order to analyze the behaviour of the spectral model in the AF remodeling scenario, it is assumed that two disjoint tissue parts exist: part A and part B. The APs generated in each tissue part are by definition different from each other, but are assumed to be the same within each set.

The measured signal spectra are therefore modelled to be dependent on the location of sensor $i$ on the tissue as

$$\mathbf{x}_i = diag(\mathbf{s})\mathbf{h}_i + \boldsymbol{\varepsilon}_i, \quad \text{where } \boldsymbol{\varepsilon}_i = \begin{cases} \mathbf{0}, & \text{if } i \in A \\ \boldsymbol{\varepsilon}_b, & \text{if } i \in B \end{cases} , \tag{3.31}$$

where $\mathbf{0}$ denotes the $F$-sized zero vector, $\mathbf{s}$ denotes the non-delayed, AP signal morphology created in tissue part A, $\boldsymbol{\varepsilon}_b$ denotes the difference between the AP signals generated in part B of the tissue compared to part A, and sets $A$ and $B$ denote the two disjoint sets of sensors in part $A$ and $B$ of the tissue respectively.

Stacking all $M$ signal spectra into the matrix $\mathbf{B}$, it can be expressed as

$$\mathbf{B} = \begin{bmatrix} \mathbf{x}_1 & \mathbf{x}_2 & \cdots & \mathbf{x}_M \end{bmatrix} = diag(\mathbf{s})\mathbf{H} + \mathbf{E} , \tag{3.32}$$

where

$$\mathbf{H} = \begin{bmatrix} \mathbf{h}_1 & \mathbf{h}_2 & \cdots & \mathbf{h}_M \end{bmatrix} \quad \text{and} \quad \mathbf{E} = \begin{bmatrix} \boldsymbol{\varepsilon}_1 & \boldsymbol{\varepsilon}_2 & \cdots & \boldsymbol{\varepsilon}_M \end{bmatrix} . \tag{3.33}$$

Note that all non-zero elements of $\mathbf{E}$ are in the columns that denote the locations that are part of set $B$ and consists of the $\boldsymbol{\varepsilon}_b$ columns. Because the matrix $\mathbf{E}$ can only consist of the column vectors $\boldsymbol{\varepsilon}_b$, the rank of $\mathbf{E}$ is therefore automatically one.

Now considering the rank of the $\mathbf{B}$ matrix, an upper limit can be obtained using the property of Equation (2.19) as

$$\text{rank}(\mathbf{B}) \leq \text{rank}(\mathbf{H}) + \text{rank}(\mathbf{E}) . \tag{3.34}$$

It is already established in Section 3.5.1 that the rank of $\mathbf{H}$ is full (or $M$). Therefore, the addition of the rank-1 $\mathbf{E}$ matrix, can, in theory, reduce the rank of the $\mathbf{B}$ matrix to be less than full-rank. However, this only happens when the addition of the $\boldsymbol{\varepsilon}_b$ vector in $\mathbf{B}$ to the linearly independent column vectors of $\mathbf{H}$ is exactly as such that they become linearly dependent. Without proof, it is expected that this is unlikely to happen, causing the $\mathbf{B}$ matrix in this scenario to be expected to be full-rank.

Now considering the absolute value of the measurements $|\mathbf{x}_i|$, the matrix $|\mathbf{B}|$ can be expressed as

$$|\mathbf{B}| = |diag(\mathbf{s})\mathbf{H} + \mathbf{E}| . \tag{3.35}$$

Now an expression for the upper limit of the rank of the $|\mathbf{B}|$ matrix needs to be obtained. Unfortunately, it is impossible to express the upper limit of the rank of $|\mathbf{B}|$ as

$$\text{rank}(|\mathbf{B}|) \leq \text{rank}(|\mathbf{H}|) + \text{rank}(|\mathbf{E}|) , \tag{3.36}$$

because $|\mathbf{B}| \neq |diag(\mathbf{s})\mathbf{H}| + |\mathbf{E}|$. Therefore, the equality is used that

$$\text{rank}(|\mathbf{B}|) = \text{rank}(|\mathbf{B}|^{\circ 2}) \tag{3.37}$$

and an expression for the matrix $|\mathbf{B}|^{\circ 2}$ is obtained as

$$|\mathbf{B}|^{\circ 2} = |diag(\mathbf{s})\mathbf{H}|^{\circ 2} + |\mathbf{E}|^{\circ 2} + diag(\mathbf{s})\mathbf{H} \odot \overline{\mathbf{E}} + \overline{diag(\mathbf{s})\mathbf{H}} \odot \mathbf{E} \ , \tag{3.38}$$

where the $\cdot^{\circ 2}$-operator denotes an element-wise power of 2, and $\odot$ denotes an element-wise multiplication.

An upper limit to the rank of $|\mathbf{B}|$ can now be obtained as

$$\begin{aligned} \text{rank}(|\mathbf{B}|) = \text{rank}(|\mathbf{B}|^{\circ 2}) \leq \text{rank}(|diag(\mathbf{s})\mathbf{H}|^{\circ 2}) + \text{rank}(|\mathbf{E}|^{\circ 2}) + \text{rank}(diag(\mathbf{s})\mathbf{H} \odot \overline{\mathbf{E}}) \\ + \text{rank}(\overline{diag(\mathbf{s})\mathbf{H}} \odot \mathbf{E}) \ , \end{aligned} \tag{3.39}$$

where it is already known that

$$\text{rank}(|diag(\mathbf{s})\mathbf{H}|^{\circ 2}) = \text{rank}(|\mathbf{H}|) = 1$$

and

$$\text{rank}(|\mathbf{E}|^{\circ 2}) = \text{rank}(|\mathbf{E}|) = 1 \ .$$

Furthermore, because for any matrix $\mathbf{X}$

$$\text{rank}(\mathbf{X}) = \text{rank}(\overline{\mathbf{X}}) \quad \text{and} \quad \overline{diag(\mathbf{s})\mathbf{H} \odot \overline{\mathbf{E}}} = \overline{diag(\mathbf{s})\mathbf{H}} \odot \mathbf{E} \ ,$$

the last two terms of Equation (3.39) are equal and the upper limit can thus be expressed as

$$\text{rank}(|\mathbf{B}|) \leq 2 + 2 \cdot \text{rank}(diag(\mathbf{s})\mathbf{H} \odot \overline{\mathbf{E}}) \ . \tag{3.40}$$

As a final step, the structure of the $\mathbf{E}$ matrix, which only has $|B|$ (cardinality of set $B$) amount of non-zero columns, is used. Because of the elementwise multiplication, this property of the $\mathbf{E}$ matrix thus also limits the rank of $diag(\mathbf{s})\mathbf{H} \odot \overline{\mathbf{E}}$ to $|B|$. This allows the upper limit of the rank of $|\mathbf{B}|$ to be written as

$$\text{rank}(|\mathbf{B}|) \leq 2 + 2|B| \ , \tag{3.41}$$

where $|B|$ denotes the cardinality of set $B$, or, in other words, the amount of sensors that measure a different magnitude signal spectrum than set $A$.

The result obtained above, where only two different AP signal shapes were assumed, can be generalized to environments where more than two different AP signal shapes are measured by replacing the cardinality of set $B$ in Equation (3.41) with the amount of sensors that measure a different AP than the reference AP signal morphology expressed by $\mathbf{s}$.

From Equations (3.34) and (3.41) it therefore is concluded that the rank of the matrix $\mathbf{B}$ is at most full-rank and is also expected to be full-rank, and that the rank of the $|\mathbf{B}|$ matrix is dependent on the amount of sensors that measure a different magnitude spectrum than the reference AP signal expressed by $\mathbf{s}$.

### 3.5.3. Ectopic foci

The last scenario will analyse the behaviour of the spectral signal model under the assumption that a homogeneous tissue is stimulated at multiple stimulation locations. Following the same reasoning as explained in the theoretical analysis of the cardiac signal model in Section 3.4.3, it is assumed that each sensor still measures exactly the same AP, but now coming from more than one stimulation location. The measured signal spectra are therefore modelled similar as in the NSR scenario as

$$\mathbf{x}_i = \mathbf{s} \odot \mathbf{h}_i = diag(\mathbf{s})\mathbf{h}_i \ , \tag{3.42}$$

where $\mathbf{s}$ still denotes the reference non-delayed AP signal and $\mathbf{h}_i$ denotes the moment of arrival of that reference AP signal. Because the vector $\mathbf{h}_i$ depends only on the time-delay $\tau_i$, Equation (3.42) can simply be extended to more stimulation location by always choosing the steering vector $\mathbf{h}_i$ that belongs to the lowest $\tau_i$. This extension does not change the expression of Equation (3.42), and because Equation (3.42) is equal to Equation (3.26) derived in Section 3.5.1, the same conclusions about the rank of the $\mathbf{B}$ and $|\mathbf{B}|$ matrices are drawn. Namely that the rank of the matrix $\mathbf{B}$ will always be full in this scenario, and the rank of the matrix $|\mathbf{B}|$ will always be one.

### 3.5.4. Conclusion theoretical analysis of spectral signal model

The theoretical analysis that is performed in this section focused on obtaining expressions for the rank of the matrices $\mathbf{B}$ and $|\mathbf{B}|$ that are both constructed from the spectral signal model that is defined in Section 3.3.2 for each of the three defined scenarios of Section 3.2.

From the performed analysis, a couple of interesting conclusions are drawn. First, it is observed that the rank of $\mathbf{B}$ will always be full, regardless of the analyzed phenomena that occur in the cardiac tissue. Therefore, no information about AF can be extracted from this metric alone using the spectral signal model.

However, when considering the rank of the $|\mathbf{B}|$ matrix, it shows interesting results, because the rank of $|\mathbf{B}|$ can vary depending on the analyzed scenario. The above analysis has namely shown that the rank of $|\mathbf{B}|$ is one, except for in the AF remodeling scenario, where the upper limit of the rank of $|\mathbf{B}|$ is dependent on the amount of different measured signals. This gives a theoretical reason for this signal model to give interesting insights about AF by analyzing the SVD of the $|\mathbf{B}|$ matrix. However, because only an upper limit of the rank of $|\mathbf{B}|$ could be obtained for the AF remodeling scenario, it has to be further investigated whether this theoretical result is useful in practice. This is done in the next section of this chapter.

Another interesting conclusion from the performed analysis is that no difference in the rank of the $\mathbf{B}$ and $|\mathbf{B}|$ matrices were found between the NSR and ectopic foci scenarios. For both of these scenarios, the model expressed by Equations (3.26) and (3.42) are namely similar. This is the same behaviour as was found for the cardiac signal model and again outlines the difference between the actual behaviour of these cardiac models and the behaviour that is expected from the general array processing signal models.

The last important conclusion from the performed theoretical analysis of this model is that the use of stochastic variables could successfully be avoided during the analysis. This makes the estimation of the $\mathbf{B}$ and $|\mathbf{B}|$ matrices practically more feasible, because no stationarity assumptions were required during the performed analysis and the analyzed matrices do not have to be estimated over multiple time frames. This essentially solves all three problems that are stated in the problem formulation (Section 3.1), which makes the application of the spectral signal model to epicardial EGM measurements to fibrillation heart tissue theoretically promising.

## 3.6. Analysis of novel signal models in AF environments using physiological simulations

In order to test the theoretical results obtained in the previous sections, a physiological simulation is performed in Matlab that calculates the eigenvalues of the autocorrelation matrix $\mathbf{R}_x(\omega)$ of the cardiac signal model and the singular values of the $\mathbf{B}$ and $|\mathbf{B}|$ matrices of the spectral signal model for the three different cardiac scenarios described in Section 3.2. A visual representation of the performed simulation methodology is shown in Figure 3.3 below.

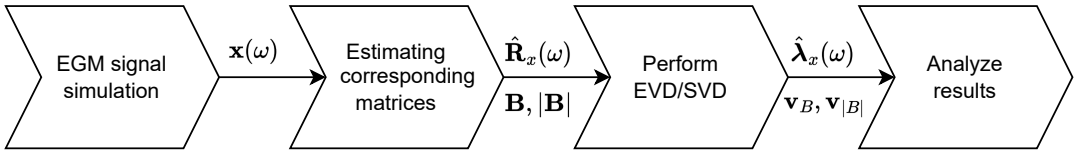


Figure 3.3: Implemented simulation methodology

This section first discusses how the physiological simulations are implemented. Thereafter, the resulting eigenvalues of the autocorrelation matrices for the cardiac signal model and the resulting singular values of the $\mathbf{B}$ and $|\mathbf{B}|$ matrices of the spectral signal model are shown respectively. The results of the physiological simulations are lastly concluded in Section 3.6.4.

### 3.6.1. Simulation implementation

The physiological simulation of the AP impulses in cardiac tissue is done using the model created by Courtemanche *et al.* [12] that is discussed in Section 2.1. The diffusion equation of Equation (2.2) is subsequently used to model the propagation of this AP between the cells. From this tissue model the EGM signals are lastly simulated using Equation (2.4). It is hereby assumed that each sensor measures the electrical activity of each simulated cell, weighted inversely with the distance to the electrode.

All simulations consider a single heartbeat on a tissue of 90 x 90 cells with a sampling frequency of 20 kHz. An EGM sensor size $M = 25$ is used for the EGM simulation and the sensors are placed in a 5-by-5 array geometry. As a last step, measurement noise is added as independent realisations from a zero-mean Gaussian random variable with variance $\sigma_n^2$, or $\mathcal{N}(0, \sigma_n^2)$. The noise variance $\sigma_n^2$ is chosen as such that an SNR of 20 dB is achieved when compared to the signal measured at the first electrode.

For each scenario a different simulation approach was implemented. Each of which is briefly discussed below.

**Scenario 1 - NSR:**
The normal sinus rhythm simulation is implemented using a single stimulation location in the top left corner of the tissue. The tissue conductivity was furthermore left homogeneous at a value of $\sigma_e = 2.4$ nS/µm/pF.

**Scenario 2 - AF remodeling**
The remodeling of the cardiac tissue is simulated by changing the cell conductivities of certain parts of the tissue to $0.01\sigma_e$. This decrease in conductivity functions as a propagation block, which radically changes the propagating path of the AP impulse. For this scenario the same stimulation location was chosen at the top left corner of the tissue. The conductivity map of this scenario is created manually and can be distinguished from the center image of Figure 3.5.

**Scenario 3 - Ectopic foci**
The existence of ectopic foci is simulated by adding another stimulation location on the tissue. This second stimulation location is on the bottom right corner of the tissue. The conductivities of the tissue are left homogeneous at $\sigma_e = 2.4$ nS/µm/pF.

**Simulation results:**
The resulting signals that are simulated using the methodology described above are shown below in Figures 3.4 to 3.6.

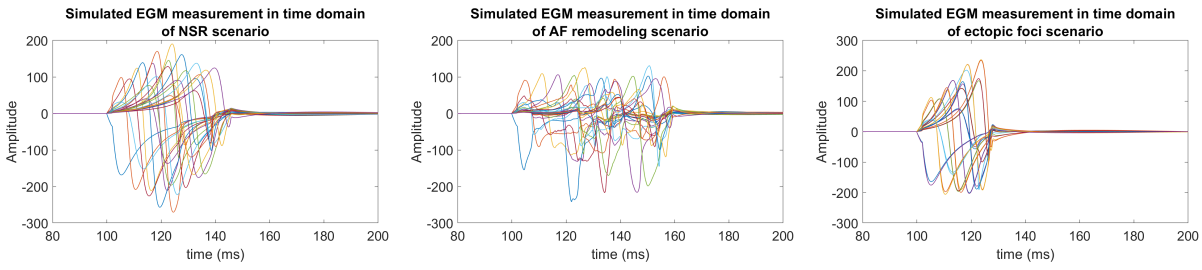


Figure 3.4: Simulated time domain EGM signal for all $M$ electrodes.

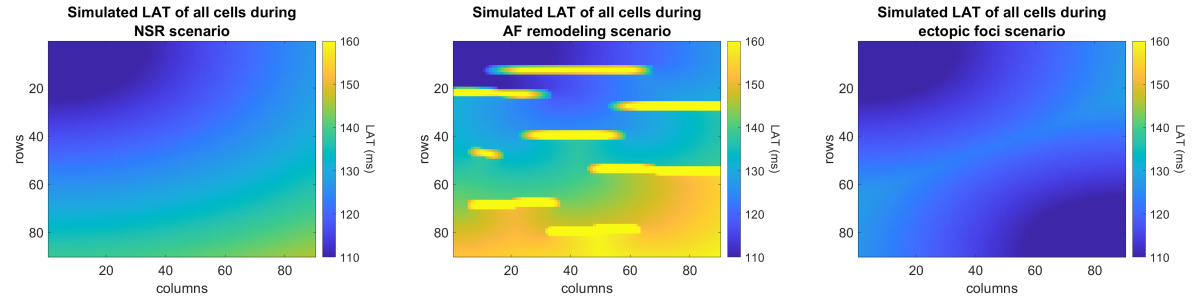


Figure 3.5: LAT of all 90 by 90 simulated cells.

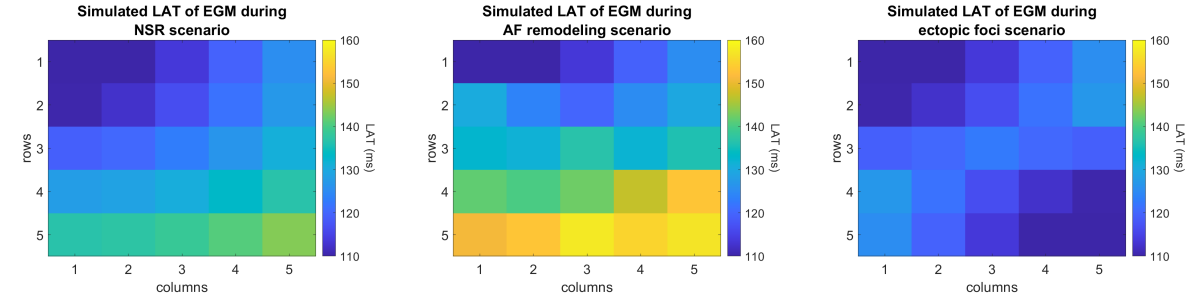


Figure 3.6: LAT of each EGM electrode.

### Constructing matrices

Using the simulated EGM measurements, the autocorrelation matrix for each frequency bin $\mathbf{R}_x(\omega)$ is calculated. This is done by first framing the measurements into $K_w$, 50%-overlapping Hamming windows. Each window is subsequently transformed to the frequency domain using an FFT. Within the frequency domain the autocorrelation matrix for each frequency $\mathbf{R}_x(\omega)$ is then estimated as

$$\hat{\mathbf{R}}_x(\omega) = \frac{1}{K_w} \sum_{i=0}^{K_w-1} \mathbf{x}(\omega, i)\mathbf{x}(\omega, i)^H \ , \tag{3.43}$$

where $\mathbf{x}(\omega, i)$ is the measurement vector of size $M$ for frequency bin $\omega$ and the $i$th timeframe. Four different values for the amount of time frames $K_w$ are hereby applied to explore the impact this metric has on the results.

To construct the $\mathbf{B}$ matrix, the $M$ simulated EGM signals are first transformed into the frequency domain as a whole, so without framing and windowing, and are subsequently stacked columnwise into the $\mathbf{B}$ matrix as described in Equation (3.24). Only the frequencies between 0 Hz and 100 Hz are hereby taken into account.

The $|\mathbf{B}|$ matrix is lastly constructed by calculating the absolute value of every element in the $\mathbf{B}$ matrix.

### Analysing the EVD and SVD of matrices

The last step of the simulation analysis entails obtaining the eigenvalues and singular values of the constructed $\mathbf{R}_x$, $\mathbf{B}$, and $|\mathbf{B}|$ matrices. This is done in Matlab using the build-in eig() and svd() functions. The eigenvalues and singular values are subsequently sorted from largest to smallest. Lastly, the eigenvalues and singular values are normalized to the first, largest value as

$$\lambda_i = \frac{\lambda_i}{\lambda_1} \ , \tag{3.44}$$

where $\lambda_i$ denotes the $i$th singular- or eigenvalue.

### 3.6.2. Simulation results cardiac system model

Using the methodology described above, the eigenvalues of the autocorrelation matrices of the cardiac signal model are simulated for all three discussed scenarios. In these simulations four different amount of time frames $K_w \in \{4, 10, 20, 40\}$ are used to show the dependence of the eigenvalue pattern on this parameter. The results are shown below in Figures 3.7 to 3.10.

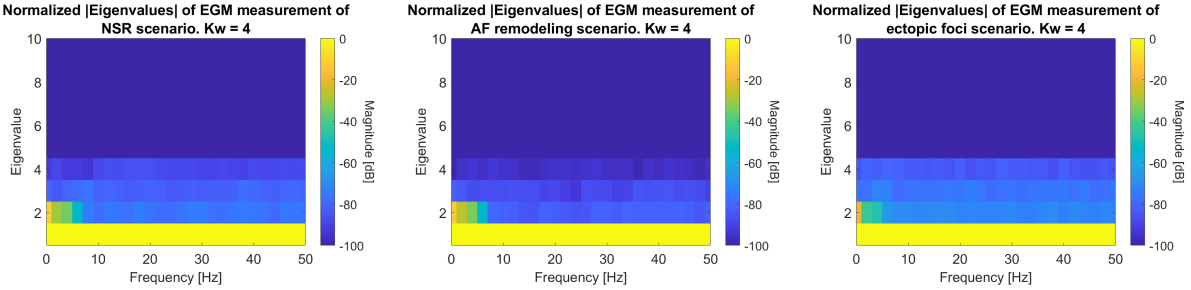


(a) NSR scenario (b) AF remodeling scenario (c) Ectopic foci scenario

Figure 3.7: Resulting eigenvalue patterns of each scenario for frequencies $0 < \omega < 50$Hz with amount of time frames $K_w = 4$. Only the first 10 eigenvalues are depicted.

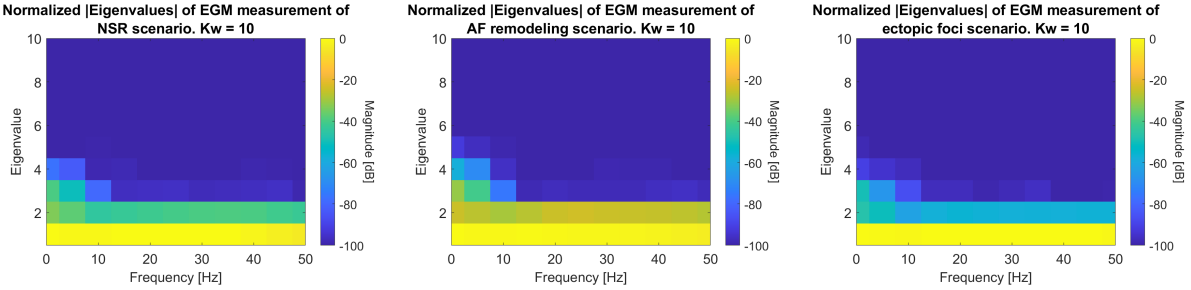


(a) NSR scenario (b) AF remodeling scenario (c) Ectopic foci scenario

Figure 3.8: Resulting eigenvalue patterns of each scenario for frequencies $0 < \omega < 50$Hz with amount of time frames $K_w = 10$. Only the first 10 eigenvalues are depicted.

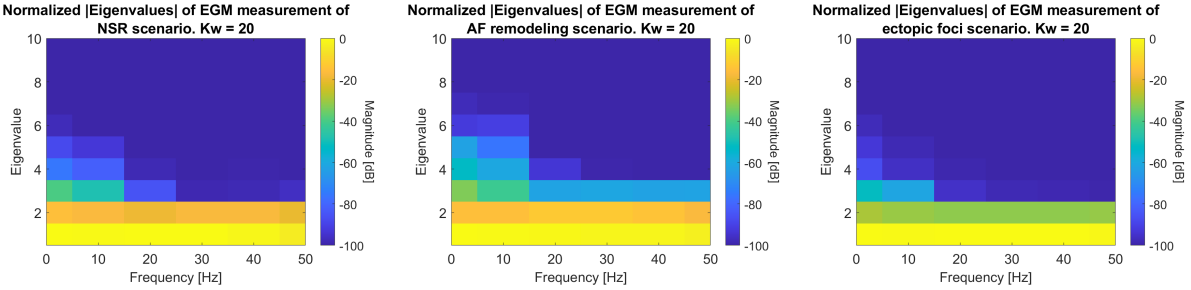


(a) NSR scenario (b) AF remodeling scenario (c) Ectopic foci scenario

Figure 3.9: Resulting eigenvalue patterns of each scenario for frequencies $0 < \omega < 50$Hz with amount of time frames $K_w = 20$. Only the first 10 eigenvalues are depicted.

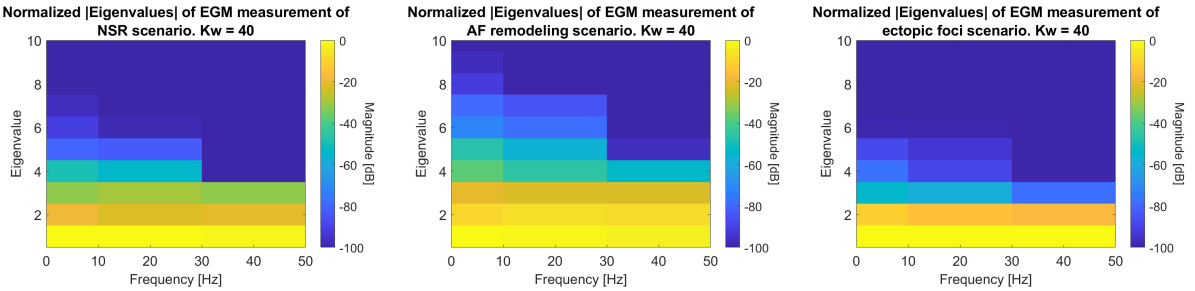


(a) NSR scenario (b) AF remodeling scenario (c) Ectopic foci scenario

Figure 3.10: Resulting eigenvalue patterns of each scenario for frequencies $0 < \omega < 50$Hz with amount of time frames $K_w = 40$. Only the first 10 eigenvalues are depicted.

When analyzing the results presented in this section, a couple of observations are made. First, the amount of large eigenvalues seems to increase with the chosen amount of time frames $K_w$. Secondly, the amount of large eigenvalues of the AF remodeling scenario is consistently equal to or higher than in the NSR scenario. Thirdly, the amount of large eigenvalues of the ectopic foci scenario is consistently equal to or smaller than in the NSR scenario. Lastly, the differences between the scenarios seem to decrease as the length of the time frames increases ($K_w$ decreases).

All these observation can be explained by the non-ideal effects of estimating the autocorrelation matrix. Specifically the length and amount of time frames seem to have a big effect on the presented results. Equation (3.43) shows that each timeframe can only add a rank-1 contribution to $\hat{\mathbf{R}}_x(\omega)$. By increasing $K_w$, the length of each time frame becomes smaller, which increases how many time frames overlap with the AP impulse on the EGM. The high energy signal of the AP impulse, combined with the different shapes of the EGM signal between the time frames, results in a new linearly independent eigenvector with a significantly large corresponding eigenvalue. Thus, the more time frames overlap with the impulse, the higher the amount of large eigenvalues of $\hat{\mathbf{R}}_x$ will be. This also explains why the amount of large eigenvalues in the AF remodeling scenario is consistently higher: The impulse takes longer (as Figure 3.4b shows), thus more time frames overlap with the impulse. The opposite effect explains the consistently lower amount of large eigenvalues of the ectopic foci scenario; it is because the impulses last shorter in this scenario.

These effects are the result of the stationarity assumption of the cardiac signal model that can not be held in this application. The autocorrelation matrix expressions of Section 3.4 assume that the measured signals between the time frames are stationary, and that statistically independent variations of the sources between the time frames increase the rank of the autocorrelation matrix. In practice however, this assumption does not work, because the cardiac electrical impulses are guaranteed not to be stationary with one heartbeat, and even across multiple heartbeats stationarity is not likely, especially when arrhythmia are present. This unavoidably leads to the results in which the theoretical autocorrelation matrix can not properly be estimated and no significant differences between the scenarios can be distinguished.

### 3.6.3. Simulation results spectral signal model

The spectral signal model is analyzed using the same physiological simulations as for the cardiac signal model. However, now the $\mathbf{B}$ and $|\mathbf{B}|$ matrices are used to extract information about AF. These matrices are simulated for the three scenarios discussed in Section 3.2. The resulting normalized singular values of the matrices are shown below in Figures 3.11a and 3.11b.

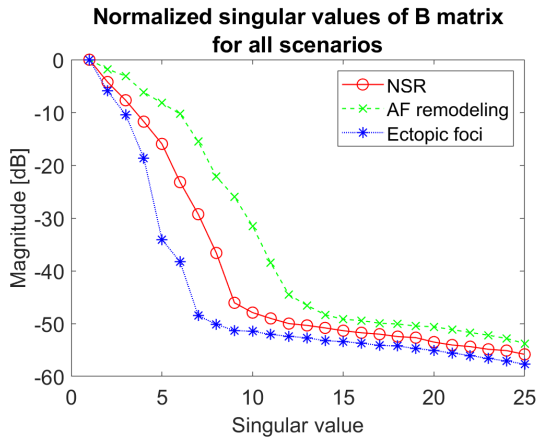


(a) Normalized singular values of the $\mathbf{B}$ matrix.

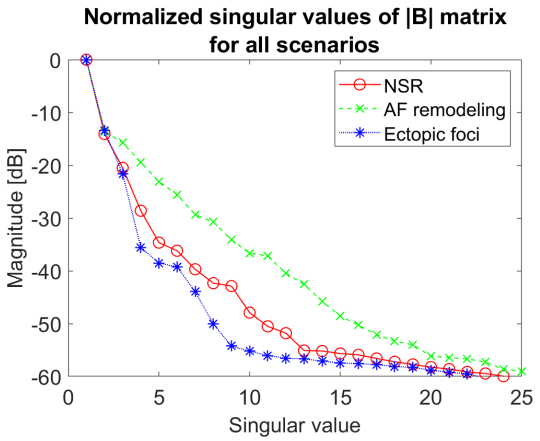


(b) Normalized singular values of the $|\mathbf{B}|$ matrix.

Figure 3.11: Results of the physiological simulation analysis of the $\mathbf{B}$ and $|\mathbf{B}|$ matrices from the spectral signal model. Results are obtained with an SNR of 20 dB.

From the theoretical analysis performed in Section 3.5 it was expected that the $\mathbf{B}$ matrix always is full-rank and the $|\mathbf{B}|$ matrix is rank-1, except for in the AF remodeling scenario, where it can become a higher rank. Analyzing the singular values presented in Figure 3.11, a clear distinction of the singular value patterns between the scenarios is observed across both figures. The singular values of the ectopic foci scenario are namely consistently the lowest, and the singular values corresponding to the AF remodeling scenario are consistently the highest. This observation can currently not yet be fully explained. It is possible that this result is caused by a difference in total signal energy, or impulse duration of the EGM measurements between the scenarios. It might be an interesting topic for future research to explore this effect further and whether it can provide information about AF from EGM measurements. According to the theoretical analyses of Sections 3.4 and 3.5, no such theoretical foundation has as of yet been found. This observation on its own is therefore not used to validate the theoretical analysis.

However, a more interesting observation of the results can be found in the comparison between the shapes of the singular values between the two figures. The singular values of the $\mathbf{B}$ matrix presented in Figure 3.11a namely in general seem to increase in negative slope, while the singular values of the $|\mathbf{B}|$ matrix gradually seem to decrease in negative slope. This overall increase in slope as shown in Figure 3.11a is believed to indicate a higher rank matrix, and the overall decrease in slope of Figure 3.11b to indicate a lower rank matrix.

Analyzing the singular values of the $\mathbf{B}$ matrix further, it seems that the shape of the singular value pattern for each scenario is very similar, although the singular values from the AF remodeling scenario consistently have a higher amplitude. This consistency in shape is believed to indicate that all $\mathbf{B}$ matrices are of a high rank, as would also be suggested by the theoretical analysis of Section 3.4.

When analyzing the singular values of the $|\mathbf{B}|$ matrix, the distinction in the shape between the AF remodeling scenario and the other scenarios is more apparent. The shape of the singular values in Figure 3.11b corresponding to the NSR and ectopic foci scenarios is comparable to a negative exponential function shape, while the AF remodeling singular values seem to decrease more linearly. This difference indicates that the $|\mathbf{B}|$ matrix from the AF remodeling scenario is of a higher rank than the $|\mathbf{B}|$ of the NSR and ectopic foci scenarios, especially when considering that the singular values are expressed in logarithmic scale. This observation also agrees with the performed theoretical analysis of Section 3.5 and shows the potential in using the singular values of the $|\mathbf{B}|$ matrix as a classification feature for AF.

### 3.6.4. Conclusion of physiological simulations

The main goal of the physiological simulations was to validate the theoretical analysis that is performed in Sections 3.4 and 3.5. This is done by simulating the epicardial, atrial EGM measurements using its physiological mechanisms and then applying the knowledge of the two defined signal models of Section 3.3 to these measurements. From the presented results, the physiological simulations seem to

agree with the performed theoretical analysis, even though the assumption was made in the theoretical analysis that each sensor only measures one AP of the cell directly underneath the sensor. As was expected and is also apparent from Figure 3.4, this assumption is incorrect. However, because the obtained expressions of the theoretical analyses are only dependent on signal shapes, they can relatively easily be generalized to also agree with the spatially averaged EGM sensor measurements.

This leads to the conclusion that the performed physiological simulations validate the theoretical results, which state that the eigenvalue pattern of the autocorrelation matrix of the cardiac signal model is expected to give little insight into AF from epicardial EGM measurements, while the spectral signal model can be used to construct matrices of which the rank is correlated to AF.

## 3.7. Chapter conclusion

In this chapter a closer look at the theoretical understanding of applying a signal model to cardiac EGM measurements is obtained. This is done by first discussing why the ideas behind the general signal model of the literature are theoretically incompatible with cardiac AP impulse propagation. From this observation two updated signal models are subsequently derived that should theoretically be more compatible with the cardiac environment. These two defined models are the cardiac signal model, which can be considered a generalization of the general signal model, and the spectral signal model, which expresses the entire measured spectra. These two signal models are analyzed to investigate their behaviour under different cardiac environments. From the three performed analyses presented above, it is concluded that the amount of large eigenvalues of both the autocorrelation and autocovariance matrices of the cardiac signal model is expected to give little useful information regarding AF from epicardial EGM measurements, because the non-ideal effects from estimating the autocorrelation matrix can not be neglected and are too influential. Therefore, although the first two problems of the problem formulation (Section 3.1) could be solved by the cardiac signal model and the model is thus in theory able to accurately depict cardiac impulse propagation, the third problem still causes the application of this signal model to be troublesome for the investigated application.

The $\mathbf{B}$ and $|\mathbf{B}|$ matrices of the second signal model however, the spectral signal model, can be estimated from a single time frame, solving the main problem of the cardiac signal model. From the performed analyses of that signal model it is concluded that this model successfully solves all three problems posed in the problem statement. The analyses of this model also show that the $|\mathbf{B}|$ matrix of this model can be used to detect AF from epicardial EGM measurements, although more research is still required to bring the current theory into practice. The spectral signal model also seems to be able to properly represent the cardiac impulses. This ability, with the fact that it can provide useful information from a single heartbeat, led to the example application discussed in the next chapter. Here, the model is used to estimate the local activation times (LAT) of the cells underneath each electrode.

# 4

# Estimating LAT using signal spectra

In the previous chapter an in-depth analysis is performed to investigate the behaviour of multiple signal models applied to epicardial EGM measurements. The chapter concludes that the cardiac signal model shows limited practical potential in the investigated applications of AF, especially when limiting the measurements to a single heartbeat. However, the spectral signal model could satisfy all three problems posed by the problem formulation in Section 3.1, also with measurements taken from a single heartbeat. The large potential that comes with this conclusion is exemplified in this chapter, where the spectral signal model is applied to a practical estimation problem that is desired for AF diagnostics: estimating the local activation times (LAT) of the cells.

To achieve this, first the spectral signal model is summarized again in Section 4.1 for readability purposes. Thereafter, the exact research question this chapter investigates is discussed in Section 4.2. The novel algorithms to solve the problem are subsequently discussed in Section 4.3 and the validation process of the designed algorithms is explained in Section 4.4. The results of the validation are lastly enumerated in Section 4.5 from which the final conclusion of this chapter is drawn that is depicted in Section 4.6.

## 4.1. Used signal model

The spectral signal model that is defined in Section 3.3.2 is used in this chapter to estimate the LAT of the cells underneath each electrode. This spectral signal model expresses the measured signal spectrum of sample size $F$ from electrode $i$ as

$$\mathbf{x}_i = \mathbf{s} \odot \mathbf{h}_i + \boldsymbol{\varepsilon}_i + \mathbf{n} = diag(\mathbf{s})\mathbf{h}_i + \boldsymbol{\varepsilon}_i + \mathbf{n} \,, \tag{4.1}$$

where $\mathbf{s}$ denotes the reference, non-delayed AP signal spectrum, $\mathbf{h}_i$ denotes the transfer function that delays the signal $\mathbf{s}$ to the $i$th electrode, the $\odot$-operator denotes the element-wise vector product, $\boldsymbol{\varepsilon}_i$ represents the sensor-specific deviations from the reference spectrum $\mathbf{s}$, and $\mathbf{n}$ denotes the measurement noise. The measurement noise $\mathbf{n}$ is assumed to be independent realisations of a zero-mean complex Gaussian stochastic variable. The $\mathbf{h}_i$ vector still is assumed to have the form

$$\mathbf{h}_i = \zeta_i \begin{bmatrix} 1 \\ e^{j2\pi\frac{1}{F}\tau_i} \\ e^{j2\pi\frac{2}{F}\tau_i} \\ \vdots \\ e^{j2\pi\frac{F-1}{F}\tau_i} \end{bmatrix} = \zeta_i \begin{bmatrix} 1 \\ \phi_i \\ \phi_i^2 \\ \vdots \\ \phi_i^{F-1} \end{bmatrix}, \quad \text{with } \phi_i = e^{j2\pi\frac{1}{F}\tau_i} \,, \tag{4.2}$$

In this chapter, instead of considering $\mathbf{s}$ as a reference AP, it is considered as a reference EGM impulse. This reference EGM impulse is subsequently delayed to each sensor. Other effects that occur through the spatial averaging of APs to the electrode are hereby not taken into account. Note that the desired

parameter for estimation is the single $\tau_i$ variable in the steering vector $\mathbf{h}_i$, because it denotes the time-delay from the reference impulse to the $i$th sensor, which corresponds to the activation time of the measured signal at sensor $i$.

## 4.2. Problem formulation

The goal of this chapter is to exemplify a practical application of the spectral signal model by estimating the LAT of the cells using a novel LAT estimation algorithm based on the spectral signal model defined in section 3.3.2 and summarized again in the previous section. An estimation of the LAT of the tissue underneath the EGM sensors hereby needs to be obtained by estimating the variable $\tau_i$ in the steering vector $\mathbf{h}_i$.

The accuracy of the novel LAT estimation algorithm will subsequently be compared with the two state of the art LAT estimation algorithms discussed in Section 2.3.2: the steepest deflection (SD) algorithm and the NCC-2 algorithm developed by Kölling *et al.* [32].

## 4.3. Methodology

In order to apply the spectral signal model to this LAT estimation problem, three implementations of the existing ESPRIT algorithm are formulated. The first implementation being a pure, unchanged application of ESPRIT on the EGM data, and the second and third being an extended version of ESPRIT. What ESPRIT entails and how it is applied to the formulated problem is the topic of this section.

### 4.3.1. ESPRIT algorithm

According to Roy and Kailath [42], ESPRIT (Estimation of Signal Parameters via Rotational Invariance Techniques) is an algorithm designed for array processing applications that uses the inherent shift-invariance structure of the sensor array. This shift-invariance property can be exploited to obtain different signal parameter estimates from the data, such as angle of arrival, time-delay, and frequency [42].

First a general description of the ESPRIT algorithm will be given based on the article of Roy and Kailath [42]. This description is thus not yet applied to the formulated problem of this chapter, but solely is depicted as an explanation of the ESPRIT algorithm. After the general ESPRIT algorithm is explained, the application of the ESPRIT method to the spectral signal model defined in Section 4.1 is discussed.

**General ESPRIT algorithm description**

In order to describe the algorithm it is convenient to split a sensor array into two subarrays of equal size $M$: $\mathbf{Z}_x$ and $\mathbf{Z}_y$, which are identical to each other except for a physical displacement. The signals received at each subarray can now be expressed using the typical array processing signal model as

$$\begin{aligned} \mathbf{x}(t) &= \mathbf{A}\mathbf{s}(t) + \mathbf{n} \\ \mathbf{y}(t) &= \mathbf{A}\mathbf{\Phi}\mathbf{s}(t) + \mathbf{n}\ , \end{aligned} \tag{4.3}$$

where $\mathbf{A} \in \mathbb{C}^{M\times d}$ is the steering matrix that steers the $d$ source signals $\mathbf{s}(t) \in \mathbb{C}^{d\times 1}$ to the $M$ sized measurement vectors $\mathbf{x}(t)$ and $\mathbf{y}(t)$, and $\mathbf{n}$ denotes independent random measurement noise. The diagonal matrix $\mathbf{\Phi} \in \mathbb{C}^{d\times d}$ denotes the difference in attenuation and time delay of the source signal between the two subarrays, due to their physical displacement. This matrix can be expressed as

$$\mathbf{\Phi} = \begin{bmatrix} \phi_0 & & & \\ & \phi_1 & & \\ & & \ddots & \\ & & & \phi_{d-1} \end{bmatrix}, \tag{4.4}$$

where $\phi_i$ denotes the extra attenuation and time delay for the $i$th source signal to travel to the subarray $\mathbf{Z}_y$, compared to $\mathbf{Z}_x$.

Stacking the measurements $\mathbf{x}$ and $\mathbf{y}$ in a vector $\mathbf{z}$ allows it to be written as

$$\mathbf{z} = \begin{bmatrix} \mathbf{x} \\ \mathbf{y} \end{bmatrix} = \tilde{\mathbf{A}}\mathbf{s}(t) + \mathbf{n}_z \tag{4.5}$$

with

$$\tilde{\mathbf{A}} = \begin{bmatrix} \mathbf{A} \\ \mathbf{A}\boldsymbol{\Phi} \end{bmatrix}. \tag{4.6}$$

Denoting the subspace spanned by the columns of $\tilde{\mathbf{A}}$ as $\mathbf{U}_z$, which can be estimated from the data, the parameter matrix $\boldsymbol{\Phi}$ can be estimated from the EVD of

$$\mathbf{U}_x^{\dagger}\mathbf{U}_y = \mathbf{T}^{-1}\boldsymbol{\Phi}\mathbf{T}\ , \tag{4.7}$$

where $\mathbf{U}_x$ and $\mathbf{U}_y$ are the first and last $M$ rows of $\mathbf{U}_z$ respectively, and $^{\dagger}$ denotes the Moore-Penrose pseudo-inverse operator. The eigenvalues of $\mathbf{U}_x^{\dagger}\mathbf{U}_y$ thus represent the estimated values $\hat{\phi}_0, \hat{\phi}_1, \ldots, \hat{\phi}_{d-1}$.

The exploitation of the structure of $\tilde{\mathbf{A}}$ to obtain an estimate of $\boldsymbol{\Phi}$ is considered the core mechanism of the ESPRIT algorithm.

**ESPRIT algorithm applied to AF signal spectrum model**

Applying the above technique to the spectral signal model as described by Equation (4.1), it is first assumed that all measured signal spectra are purely time-delayed versions of each other. Therefore the sensor-specific deviation vector $\boldsymbol{\varepsilon} = \mathbf{0}$ in Equation (4.1). The desired ESPRIT structure of Equation (4.6) can now be found in the measurements via the steering vector $\mathbf{h}_i$. To obtain the estimate of the steering vector $\mathbf{h}_i$, the following minimization problem is formulated:

$$\min_{\mathbf{h}_i} \quad E\left[\left\|\mathbf{x}_i - diag(\mathbf{s})\mathbf{h}_i - \mathbf{n})\right\|_2^2\right] \quad , \tag{4.8}$$

where $\mathbf{x}_i$ is the measured signal at sensor $i$, $\mathbf{s}$ is a reference AP signal shape, $\mathbf{h}_i$ the steering vector as depicted in Equation (3.9), and $\mathbf{n}$ the measurement noise. The measurement noise is assumed to be independent realisations of a zero-mean complex stochastic variable.

Solving this minimization problem leads to the optimal steering vector estimate

$$\hat{\mathbf{h}}_i = diag(\mathbf{s})^{-1}\mathbf{x}_i\ . \tag{4.9}$$

Note that this expression can be regarded as a deconvolution operation between signals $\mathbf{s}$ and $\mathbf{x}_i$ in the frequency domain.

Now a choice for the reference signal shape $\mathbf{s}$ needs to be made. It is theoretically possible to use a standard, a priori EGM AP impulse shape for this variable, but for the purposes of this thesis the choice is made to use the first sensor signal $\mathbf{x}_1$ as reference. This leads to the estimate $\hat{\mathbf{h}}_{1i}$ being a relative transfer function between the first sensor and sensor $i$. Incorporating this decision in the equation above leads to the final expression for the estimate $\hat{\mathbf{h}}_{1i}$ as

$$\hat{\mathbf{h}}_{1i} = diag(\mathbf{x}_1)^{-1}\mathbf{x}_i\ , \tag{4.10}$$

where $\hat{\mathbf{h}}_{1i}$ denotes the estimate of the relative transfer function that describes the delay of the AP signal from sensor 1 to sensor $i$. The structure of $\mathbf{h}_{1i}$ can be expressed as

$$\mathbf{h}_{1i} = \zeta_{1i}\begin{bmatrix} 1 \\ \phi_i \\ \phi_i^2 \\ \vdots \\ \phi_i^{F-1} \end{bmatrix}, \quad \text{with } \phi_i = e^{j2\pi\frac{1}{F}\tau_{1i}}\ , \tag{4.11}$$

where $\zeta_{1i}$ denotes a possible relative attenuation that is uniform over the entire spectrum, $\tau_{1i}$ denotes the relative time delay between the signal from sensor 1 to sensor $i$, and $F$ denotes the sample size of the spectra.

With the estimate of the relative transfer function, the ESPRIT algorithm can be applied. This is done by splitting the vector $\mathbf{h}_{1i}$ into two overlapping vectors $\mathbf{h}_x$ and $\mathbf{h}_y$, as depicted in Figure 4.1

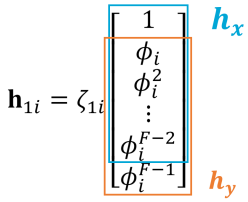


Figure 4.1: Splitting the relative transfer function $\mathbf{h}_{1i}$ into two overlapping vectors $\mathbf{h}_x$ and $\mathbf{h}_y$

Observe that the following relation between $\mathbf{h}_x$ and $\mathbf{h}_y$ now applies:

$$\mathbf{h}_y = \mathbf{h}_x \phi_i \ , \tag{4.12}$$

where $\mathbf{h}_x$ is the vector containing the top $F-1$ elements of $\mathbf{h}_{1i}$, $\mathbf{h}_y$ the vector containing the bottom $F-1$ elements of $\mathbf{h}_{1i}$, and $\phi_i = \zeta_{1i} e^{j2\pi \frac{1}{F} \tau_{1i}}$ contains the corresponding relative attenuation $\zeta_{1i}$ and time delay $\tau_{1i}$ of the entire AP.

Using the relation of Equation (4.12), an estimate of the relative $\phi_i$ between sensor 1 and $i$ can be obtained as

$$\hat{\phi}_i = \mathbf{h}_x^{\dagger} \mathbf{h}_y \ , \tag{4.13}$$

where $\mathbf{h}_x$ and $\mathbf{h}_y$ are the top and bottom subvectors of the estimated relative transfer function $\hat{\mathbf{h}}_{1i}$ respectively.

The final estimate for the relative time delay $\tau_{1i}$ between the first and $i$th sensor can now be calculated from $\hat{\phi}_i$ as

$$\hat{\tau}_{1i} = \angle(\hat{\phi}_i) \frac{F}{2\pi} \ , \tag{4.14}$$

where $\angle(\hat{\phi}_i)$ denotes the angle of $\hat{\phi}_i$ with the positive real axis in the complex plane.

By applying this method to each measured signal spectrum $\mathbf{x}_i$, the relative time delay between all sensors to the first sensor can be found. This concludes the implemented method of the ESPRIT algorithm in this thesis. This implementation of ESPRIT is referred to as the unmodified ESPRIT implementation. The extended ESPRIT implementation is described in the next section.

### 4.3.2. ESPRIT algorithm extension

Next to implementing the unmodified ESPRIT algorithm that is described in the section above, this algorithm is also extended to be better applicable to AF environments. The unmodified ESPRIT algorithm namely relies on the assumption that the signal shapes of $\mathbf{x}_1$ and $\mathbf{x}_i$ are merely time delayed and equal on all other fronts. In other words, the assumption is made that $\boldsymbol{\varepsilon} = \mathbf{0}$. In practice this will most likely not be the case, especially during AF. This will cause the spectral deconvolution step of Equation (4.10) to become inaccurate and the estimate of the relative transfer function $\hat{\mathbf{h}}_{1i}$ will not contain the desired structure.

Therefore, the addition of an extra separation step that splits the signal spectra into $k$ disjoint sets before the ESPRIT algorithm is proposed. This leads to the following three step process:

1. Classify the $M$ signal spectra into $k$ disjoint sets of similar morphology.
2. Perform the ESPRIT algorithm separately on each set.
3. Merge the sets.

Each step is further explained below.

This methodology mostly relies on the hypothesis that the signal shape variations between the sensors are discrete and can therefore be categorized into the $k$ different sets of signal shapes.

**Step 1 - Separating into k disjoint sets**

In this step the signal shapes coming from the $M$ different sensors need to be separated into $k$ disjoint sets with the goal to combine similar looking signal shapes in each set. This signal classification is

done using only the magnitude of the measured signal spectra, disregarding the phase information. In other words, how to find $k$ disjoint sets $\mathcal{S}_j \subseteq \mathcal{A}$ where $\mathcal{A} = \{1, 2, \dots, M\}$ is the whole set containing all sensors as such that the magnitude spectra from each sensor in $\mathcal{S}_j$ are most similar?

Two methods were implemented that might achieve this goal:

- Classification based on the k-means clustering algorithm
- Classification based on dot product similarity

The k-means clustering classification algorithm is an old and popular algorithm that aims to partition the $M$ measurement vectors $|\mathbf{x}_i|$ into $k$ sets by minimizing the Euclidian distances between each vector to the mean of the sets. Algorithm 1 shows the pseudo-code of the implemented k-means algorithm, based on Loyd's algoritm.

**Algorithm 1** K-means clustering algorithm. Source: [43], [44]

**Require:** $\mathbf{x}_1, \mathbf{x}_2, \dots, \mathbf{x}_M \in \mathbb{R}^F$ ▯ Denote the measured magnitude spectra
**Ensure:** $\boldsymbol{\mu}_1, \boldsymbol{\mu}_2, \dots, \boldsymbol{\mu}_k \in \mathbb{R}^F$ ▯ Initialize the $k$ cluster centers
  $i \leftarrow \{1, 2, \dots, M\}$
  $j \leftarrow \{1, 2, \dots, k\}$
  **repeat**
    **for all** $i$ **do**
      $c(i) := \arg\min_j \left\|\mathbf{x}_i - \boldsymbol{\mu}_j\right\|_2$ ▯ Assign cluster labels based on Euclidian distance
    **end for**
    **for all** $j$ **do**
      $\boldsymbol{\mu}_j := \frac{1}{\sum_p 1} \sum_p \mathbf{x}_p, \quad \forall p$, where $c(p) = j$ ▯ Calculate new cluster centers
    **end for**
  **until** no more label changes or maximum amount of iterations is reached

The dot-product based classification method is created for the purposes of this thesis and uses the inner product, or dot product, as a metric to quantify the similarity between two vectors. By calculating the dot product between the magnitude spectra for all $M$ sensor combinations with the reference sensor, a division between similar and non-similar magnitude spectra can be made. The threshold between similar and non-similar spectra is hereby based on the median of the obtained inner products, thus splitting the distribution of dot products in half.

By doing this division $k - 1$ times, $k$ disjoint sets can hereby be achieved. The created dot-product classification algorithm is described below in Algorithm 2.

**Algorithm 2** Dot-product separation algorithm into $k$ sets

**Require:** $\mathbf{x}_1, \mathbf{x}_2, \dots, \mathbf{x}_M \in \mathbb{R}^F$ ▯ Denote the measured magnitude spectra
  $i \leftarrow \{1, 2, \dots, M\}$ ▯ Set containing all sensors
  $j \leftarrow \{1, 2, \dots, k-1\}$
  **for all** j **do**
    **for all** i **do**
      $p(i) \leftarrow \mathbf{x}_1 \cdot \mathbf{x}_i$ ▯ Calculate dot product of all sensor spectra of set $i$
    **end for**
    $\text{thres} \leftarrow \text{median}(p)$ ▯ Calculate threshold
    $S(j) \leftarrow \{i \mid p(i) > thres\}$ ▯ $S(j)$ denotes the sensors that belong to set $j$
    $i \leftarrow i \setminus S(j)$ ▯ Remove labeled sensors from set $i$
  **end for**
  $S(k) \leftarrow i$ ▯ The last set gets all remaining sensors

Both algorithm 1 and 2 result in $k$ disjoint sets of sensors, each denoted by $\mathcal{S}_j$, on which the ESPRIT algorithm can subsequently be applied to.

**Step 2 - Perform ESPRIT**
On each obtained set from the previous step, the ESPRIT algorithm as described in section 4.3.1 is performed separately in order to obtain an estimate about the relative time delays between the sensors in each set. This implementation of ESPRIT is unchanged. The estimated time delays for set $\mathcal{S}_j$ are henceforth denoted as $\boldsymbol{\tau}_j$.

**Step 3 - Merging the sets**
Now the time delays between the sensors in each set is estimated, these time delays need to be merged in order to express them to a single reference. Changing the reference sensor of a set involves simply adding an offset to all the time delays of that set. So, if the offset value between the sets can be found, the sets can be merged so that all time delays are relative to the same reference sensor. However, because the classified sets are disjoint, this problem is not unambiguous.

The proposed solution to this problem involves using the ESPRIT algorithm of the whole set $\mathcal{A}$ (containing all sensors), as done in the unmodified implementation of ESPRIT described above, as a reference from which the offsets can be estimated. The estimation of the offset $\alpha_j$ between the estimated LATs of the whole set $\boldsymbol{\tau}_{\mathcal{A}} \in \mathbb{R}^M$ and the LATs $\boldsymbol{\tau}_j \in \mathbb{R}^{|\mathcal{S}_j|}$ from subset $\mathcal{S}_j$ is done using the minimization problem

$$\hat{\alpha}_j = \arg\min_{\alpha_j} \left\| \boldsymbol{\tau}_{\mathcal{A}}(\mathcal{S}_j) - \boldsymbol{\tau}_j + \mathbf{1}\alpha_j \right\|_2^2 , \tag{4.15}$$

where $\boldsymbol{\tau}_{\mathcal{A}}(\mathcal{S}_j)$ denotes the time delays from the sensors of $\mathcal{S}_j$ obtained from the ESPRIT estimates of the whole set, and $\mathbf{1}$ denotes the all-ones column vector of size $|\mathcal{S}_j|$.

Solving this minimization problem leads to the optimal solution

$$\hat{\alpha}_j = \frac{1}{|\mathcal{S}_j|} \mathbf{1}^T (\boldsymbol{\tau}_j - \boldsymbol{\tau}_{\mathcal{A}}(\mathcal{S}_j)) , \tag{4.16}$$

where $|\mathcal{S}_j|$ is the cardinality of set $\mathcal{S}_j$, $\tau_j$ are the LATs of the sensors in set $\mathcal{S}_j$, and $\boldsymbol{\tau}_{\mathcal{A}}(\mathcal{S}_j)$ denotes the time delays from the sensors of $\mathcal{S}_j$ obtained from the whole set. Note that Equation (4.16) is simply the mean of the elements in the vector $\boldsymbol{\tau}_j - \boldsymbol{\tau}_{\mathcal{A}}(\mathcal{S}_j)$.

With the estimate $\hat{\alpha}_j$, the LATs of each set $\mathcal{S}_j$ can subsequently be offset to be referenced to the same reference sensor using

$$\hat{\boldsymbol{\tau}}_j = \boldsymbol{\tau}_j + \hat{\alpha}_j \mathbf{1} , \tag{4.17}$$

where $\hat{\boldsymbol{\tau}}_j$ contains the final estimated LATs of set $\mathcal{S}_j$ relative to the reference sensor of $\mathcal{A}$. By applying Equations (4.16) and (4.17) to all $k$ sets, the LATs of the extended ESPRIT algorithm are obtained.

## 4.4. Validation

The algorithms set out in the previous section are validated using the same physiological simulation as performed in Section 3.6. This means that three scenarios are again simulated: an NSR, AF remodeling, and ectopic foci scenario, with the same parameters as discussed in Section 3.6. From the simulated EGM measurements, independent measurement noise is subsequently added to obtain a range of SNR's. The measurement noise is simulated as independent realisations of a zero-mean Gaussian distribution with variance $\sigma_n^2$. For each SNR, the noise variance $\sigma_n^2$ is calculated as such that the desired SNR is achieved when compared to the signal power of the signal measured at the first electrode. All simulations parameters are furthermore exactly the same as outlined in Section 3.6.

After the physiological EGM signal simulation for each desired SNR, five LAT estimation techniques are applied to the measurements:

- **SD algorithm:** steepest deflection algorithm as described in Section 2.3.2
- **NCC-2 algorithm:** time-domain cross-correlation over second-order neighbours algorithm (with $P = 2$) as described in Section 2.3.2
- **ESPRIT**: the unmodified ESPRIT algorithm as described in Section 4.3.1
- **ESPRIT-kmns:** the extended ESPRIT algorithm using the k-means classification algorithm, as described in Section 4.3.2

- **ESPRIT-dots:** the extended ESPRIT algorithm using the dot product classification algorithm, as described in Section 4.3.2

For the three ESPRIT based algorithms, the EGM signals first need to be transformed into the frequency domain. This is done using the FFT (Fast-Fourier Transform) algorithm in Matlab. Subsequently, only the frequency components between 10 Hz and 100 Hz are selected to be used for the ESPRIT algorithms. The lower limit of 10 Hz is specifically chosen to filter out any low frequency components of the EGM signals and to focus the algorithms on the higher frequency signal components instead. The upper limit of 100 Hz is chosen, because it is believed that no signal information is present in higher frequency bands. After the Fourier transform, the ESPRIT algorithms can be applied as described in Sections 4.3.1 and 4.3.2.

For each of the five estimated LAT's, the mean square error (MSE) with the actual activation times of the cells is lastly calculated as

$$MSE = \frac{1}{M}\sum_{i=0}^{M-1}\left(\hat{\tau}(i) - \tau(i)\right)^2 \ , \tag{4.18}$$

where $\hat{\tau}(i)$ is the estimated LAT for sensor $i$, and $\tau(i)$ is the actual LAT of sensor $i$. The MSE is used as the final metric to compare the five different LAT estimation methods. The resulting MSE's are shown in the next section.

## 4.5. Results

Using the validation methodology outlined in the previous section, the mean square error (MSE) between the five applied LAT estimation methods and the true LAT is calculated for the three defined scenarios. The calculated MSE's are shown in Figure 4.2. Figure 4.3 shows a zoomed in version to emphasize the results in the SNR range between -15 dB and 20 dB.

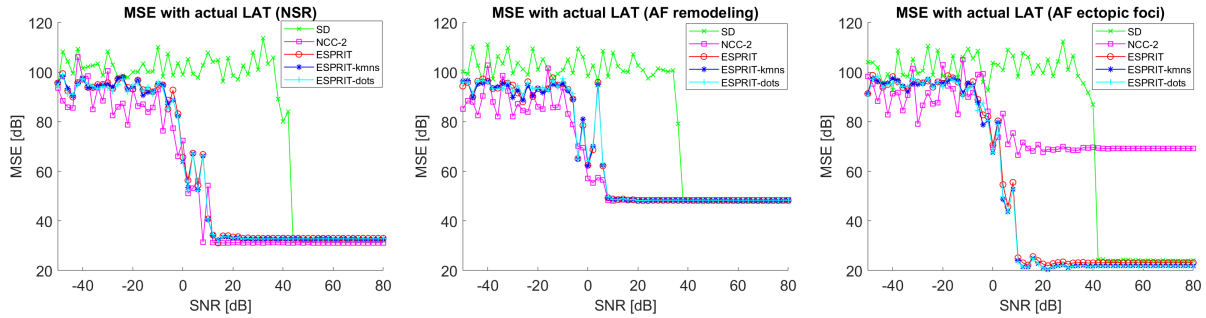


(a) NSR scenario (b) AF remodeling scenario (c) Ectopic foci scenario

Figure 4.2: Mean square error between the actual LAT and the estimated LAT from the SD, NCC-2, ESPRIT, ESPRIT-kmeans, and ESPRIT-dots algorithms for the three described scenarios.

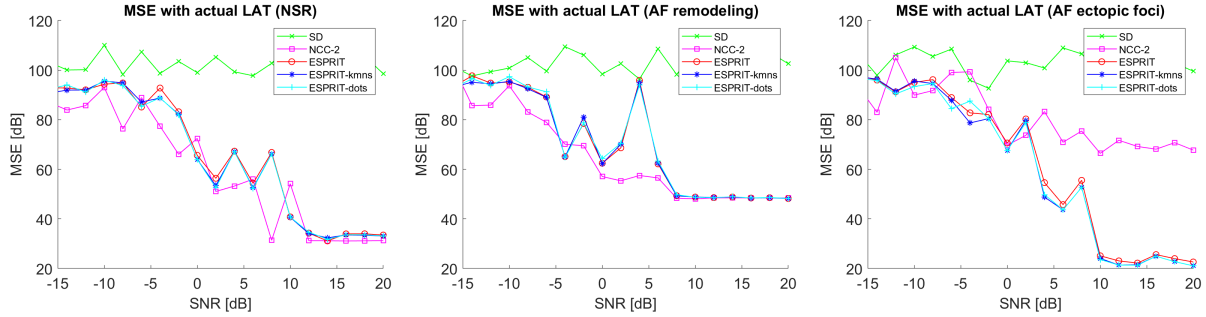


(a) NSR scenario (b) AF remodeling scenario (c) Ectopic foci scenario

Figure 4.3: Mean square error between the actual LAT and the estimated LAT from the SD, NCC-2, ESPRIT, ESPRIT-kmeans, and ESPRIT-dots algorithms for the three described scenarios zoomed in towards interesting SNR values.

From Figures 4.2 and 4.3, a couple of observations are made. Firstly, the sudden decline in accuracy of the SD algorithm that occurs around 40 dB is noticed. This shows that the SD algorithm is less resilient to high-noise conditions, which is in agreement with the literature.

Furthermore, in low-noise conditions no significant difference between the five investigated algorithms is found, except for the NCC-2 algorithm during the ectopic foci scenario. For this scenario the NCC-2 algorithm performs significantly worse than the others. An explanation for this can be that wavefronts travelling in opposite directions cause a radically different morphology from each other in the EGM signal. This can cause the time-domain cross-correlation between the electrodes to become inaccurate. This observation however needs to be investigated further to pinpoint the precise reason of this occurrence.

The accuracy of the algorithms between the different scenarios is also interesting to note. The AF remodeling scenario causes the lowest accuracy of all three scenarios, which can be explained by the high variance of signal morphologies between the sensors in this scenario. All five applied algorithms however still have a similar accuracy in low-noise conditions for this scenario, which shows that the SD algorithm for low-noise conditions is still unrivaled.

For higher noise conditions the potential of the novel ESPRIT-based algorithms become more apparent. The ESPRIT-based and NCC-2 algorithms are creating accurate results until an SNR of approximately 10 dB is reached from where the accuracy of the algorithms start to decline. During this declination, as shown in Figure 4.3, the NCC-2 algorithm seems to slightly outperform the ESPRIT-based algorithms.

It is also interesting to see that no significant difference is found between the accuracy of the implemented unmodified ESPRIT, ESPRIT-kmns, and ESPRIT-dots algorithms. Only in very rare instances do the extended ESPRIT algorithms outperform the unmodified ESPRIT estimations, and practically zero difference between the ESPRIT-kmns and ESPRIT-dots estimation accuracy is found across all presented results. This observation is further confirmed by Figure 4.4, that shows that the MSE of the ESPRIT-kmns and ESPRIT-dots algorithms are almost identical, and that the increase in the amount of sets $k$ also has little to no effect on the accuracy of the algorithms.

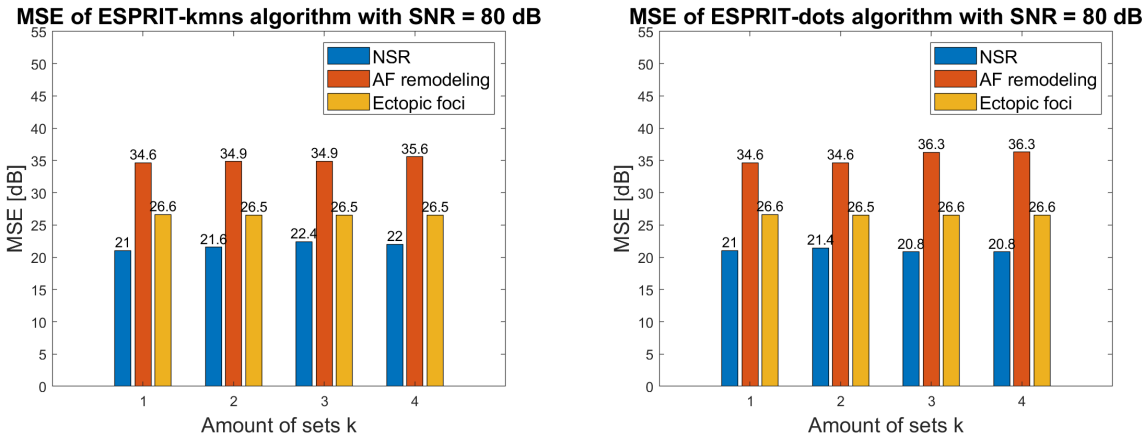


(a) ESPRIT-kmns algorithm

(b) ESPRIT-dots algorithm

Figure 4.4: MSE of extended ESPRIT algorithms vs. amount of sets $k$ with SNR = 80 dB

Lastly, the processing times of the five implemented algorithms are measured and presented in Table 4.1.

Table 4.1: Average execution times of the five implemented algorithms. Sample size of averaging is displayed in third column.

| Algorithm | Average execution time (s) | Sample size |
|---|---|---|
| **Steepest Deflection (SD)** | 0.0048 | 66 |
| **NCC-2** | 212.05 | 4 |
| **unmodified ESPRIT** | 0.018 | 66 |
| **ESPRIT-kmns** | 0.055 | 66 |
| **ESPRIT-dots** | 0.051 | 66 |

Table 4.1 shows that, although the accuracy of the NCC-2 algorithm is very high, the execution time of this algorithm is the main drawback of this algorithm. The execution times of the ESPRIT based algorithms are still significantly higher than the SD algorithm, however the argument can be made that the increase in accuracy compensates the increase in execution times. This argument is harder to make for the NCC-2 algorithm.

## 4.6. Chapter conclusion

The goal of this chapter was to exemplify an application of the spectral signal model defined in Section 3.3.2. For this purpose the choice is made to design a LAT estimation algorithm and subsequently compare that algorithm to two state of the art LAT estimation techniques that are discussed in Section 2.3.2: the SD algorithm, and the NCC-2 algorithm. For the novel estimation technique three novel approaches based on the existing ESPRIT method were formulated and subsequently validated using physiological simulations.

When comparing the results of five implemented estimation methods, it is concluded that the ESPRIT based methods perform significantly better in noisy conditions compared to the SD algorithm, although the NCC-2 algorithm still has a slight advantage in accuracy. This is however counterbalanced by the significantly longer execution time that is required for this algorithm. In low noise condition, no significant difference between the accuracy of the implemented algorithms is found, although the NCC-2 algorithm seems fundamentally incapable of accurately estimating the LAT during the ectopic foci scenario. The precise reason for this remains a topic for future research.

Lastly, the designed extensions to the unmodified ESPRIT algorithm do not seem to have significant effects on the accuracy of the algorithm. Also increasing the amount of disjoint sets $k$ seem not to have much effect. The benefits of these extensions therefore are questionable and currently do not seem beneficial to the overall estimation process.

However, the simulation results still show that it is entirely possible to create a LAT estimation algorithm based on the spectral signal model that can compete with state of the art algorithms. This shows the potential the spectral signal model has in this application and is also believed to solidify the performed analysis of the previous chapter.

# 5

# Conclusion and future work

This thesis project started with studying the application of general array processing signal models to cardiac electric impulse propagation. During this study multiple inconsistencies between the underlying mechanisms of the two systems were identified which are set out in Section 3.1. Because of these inconsistencies, it was quickly concluded that the ideas behind the general models of the literature are theoretically incompatible with cardiac AP impulse propagation. This led to the proposal of two modified signal models: the cardiac signal model and the spectral signal model. The cardiac signal model is hereby regarded as a generalization to general array processing models that incorporates the two identified fundamental system differences. The spectral signal model however takes a different approach by expressing entire signal spectra, instead of individual samples.

Chapter 3 was subsequently concerned with analyzing both models to investigate their behaviour under different cardiac environments. Especially any possible correlation between the eigenvalues of the autocorrelation matrix of the cardiac signal model, and the singular values of the $\mathbf{B}$ and $|\mathbf{B}|$ matrices of the spectral signal model with AF was hereby explored. This is done using both a theoretical analysis and a physiological simulation.

From the analysis of the cardiac signal model, it is concluded that it can represent electrical cardiac impulses better than the general signal model, although the reliance on signal stationarity make the practical potential of this signal model limited, especially when limiting the measurements to a single heartbeat. Furthermore, it is concluded that the eigenvalue pattern of the autocorrelation matrix is expected to give little useful information regarding AF from epicardial EGM measurements, also because of the stationarity assumptions of the model that can not be uphold in practice.

From the performed analyses of the spectral signal model in Chapter 3 however, it is concluded that this signal model can successfully solve all three problems posed by the problem formulation of Section 3.1. The analyses furthermore also show that the $|\mathbf{B}|$ matrix of this model can theoretically be used to classify AF from epicardial EGM measurements.

The promising results from the spectral signal model led to the example application of this model that is presented in Chapter 4. In this chapter, the spectral signal model is used as a framework to estimate the activation times of the cells. This is done by applying and modifying the existing ESPRIT methodology to this application. Three novel estimation techniques are eventually proposed in this chapter: an unmodified, direct application of ESPRIT, and two extended ESPRIT based algorithms. From the performed validation of the proposed algorithms it is concluded that the novel algorithms can compete with state of the art LAT estimation methods in terms of estimation error and execution time. This result is believed to acknowledge the performed theoretical research of this model and shows the potential benefits the spectral signal model has in the future.

## 5.1. Future work

The performed research in this thesis is mainly focused on the theoretical aspects of the analysed signal models. During this theoretical analysis, the influence of spatial averaging of AP's are mostly neglected, although it has a significant impact on the measurements. It is therefore recommended that the theoretical influence of this assumption is more precisely looked at in future research. Furthermore, next to the performed theoretical analyses, more focus can be put on the practical side of applying the proposed signal models and algorithms to epicardial EGM measurements. The application of the proposed methods to real EGM data is for example not yet investigated. The performed simulations can also be expanded to include more, and more accurate AF scenarios. Also the inclusion of a stochastic nature in the physiological simulations should be considered, with the goal to assign statistical significance to the results. Lastly, as Chapter 4 is just an example application of the spectral signal model, more applications of the explored signal models exist. These applications include but are not limited to DOA estimation of stimulation location, conduction block detection, and conduction velocity estimation.

# Bibliography


[1] World Health Organization, *Cardiovascular diseases (CVDs)*, 2023. [Online]. Available: https://www.who.int/news-room/fact-sheets/detail/cardiovascular-diseases-(cvds).

[2] E. Anter, M. Jessup, and D. J. Callans, *Atrial fibrillation and heart failure: Treatment considerations for a dual epidemic*, May 2009. DOI: 10.1161/CIRCULATIONAHA.108.821306.

[3] J. Heeringa, D. A. van der Kuip, A. Hofman, *et al.*, "Prevalence, incidence and lifetime risk of atrial fibrillation: the Rotterdam study," *European Heart Journal*, vol. 27, no. 8, pp. 949–953, Apr. 2006, ISSN: 0195668X. DOI: 10.1093/eurheartj/ehi651.

[4] S. Nattel and M. Harada, *Atrial remodeling and atrial fibrillation: Recent advances and translational perspectives*, Jun. 2014. DOI: 10.1016/j.jacc.2014.02.555.

[5] E. J. Benjamin, P. A. Wolf, R. B. D'Agostino, H. Silbershatz, W. B. Kannel, and D. Levy, "Impact of Atrial Fibrillation on the Risk of Death: The Framingham Heart Study," *Circulation*, vol. 98, no. 10, pp. 946–952, Sep. 1998. [Online]. Available: http://ovidsp.ovid.com/ovidweb.cgi?T=JS&PAGE=reference&D=ovftc&NEWS=N&AN=00003017-199809080-00003.

[6] S. Nattel, B. Burstein, and D. Dobrev, *Atrial remodeling and atrial fibrillation: mechanisms and implications*, 2008. DOI: 10.1161/CIRCEP.107.754564.

[7] S. Nattel, "New ideas about atrial fibrillation 50 years on," *Nature*, vol. 415, no. 6868, pp. 219–226, Jan. 2002, ISSN: 0028-0836. DOI: 10.1038/415219a. [Online]. Available: http://www.nature.com/articles/415219a.

[8] J. Gordon Betts, K. A. Young, J. A. Wise, *et al.*, "Cardiac Muscle and Electrical Activity," in *Anatomy and Physiology*, Houston, Texas: OpenStax, Apr. 2013, ch. 19.2. [Online]. Available: https://openstax.org/books/anatomy-and-physiology/pages/19-2-cardiac-muscle-and-electrical-activity.

[9] J. Malmivuo and R. Plonsey, *Bioelectromagnetism: Principles and Applications of Bioelectric and Biomagnetic Fields*. Oxford University Press, Mar. 2012, pp. 1–506, ISBN: 9780199847839. DOI: 10.1093/acprof:oso/9780195058239.001.0001.

[10] D. S. Lindblad, C. R. Murphey, J. W. Clark, and W. R. Giles, "A model of the action potential and underlying membrane currents in a rabbit atrial cell," *The American journal of physiologicy*, vol. 271, no. 4, H1666–H1696, Oct. 1996. DOI: 10.1152/ajpheart.1996.271.4.H1666.

[11] C. H. Luo and Y. Rudy, "A dynamic model of the cardiac ventricular action potential. I. Simulations of ionic currents and concentration changes.," *Circulation Research*, vol. 74, no. 6, pp. 1071–1096, Jun. 1994, ISSN: 0009-7330. DOI: 10.1161/01.RES.74.6.1071.

[12] M. Courtemanche, R. J. Ramirez, and S. Nattel, "Ionic mechanisms underlying human atrial action potential properties: insights from a mathematical model," *American Journal of Physiology - Heart and Circulatory Physiology*, vol. 275, no. 1, H301–H321, Feb. 1998.

[13] B. Abdi, R. C. Hendriks, A. J. van der Veen, and N. M. de Groot, "A compact matrix model for atrial electrograms for tissue conductivity estimation," *Computers in Biology and Medicine*, vol. 107, pp. 284–291, Apr. 2019, ISSN: 18790534. DOI: 10.1016/j.compbiomed.2019.02.012.

[14] N. Virag, V. Jacquemet, C. S. Henriquez, *et al.*, "Study of atrial arrhythmias in a computer model based on magnetic resonance images of human atria," *Chaos*, vol. 12, no. 3, pp. 754–763, 2002, ISSN: 10541500. DOI: 10.1063/1.1483935.

[15] A. van Oosterom, "Solidifying the solid angle," *Journal of Electrocardiology*, vol. 35, no. 4, pp. 181–192, Oct. 2002, ISSN: 00220736. DOI: 10.1054/jelc.2002.37176.

[16] J. Heijman, J.-B. Guichard, D. Dobrev, and S. Nattel, "Translational challenges in atrial fibrillation," *Circulation Research*, vol. 122, no. 5, pp. 752–753, Mar. 2018, ISSN: 15244571. DOI: 10.1161/CIRCRESAHA.117.311081.

[17] M. A. U. Zaman and D. Du, "A Review on Atrial Fibrillation (Computer Simulation and Clinical Perspectives)," *Hearts*, vol. 3, no. 1, pp. 20–37, Feb. 2022. DOI: 10.3390/hearts3010005.

[18] B. Abdikivanani, “Atrial fibrillation fingerprinting,” Ph.D. dissertation, Delft University of Technology, Delft, Oct. 2021, ISBN: 978-94-6384-260-0. DOI: 10.4233/uuid:af53215c-69ea-4c18-8761-d5cfd2c6e186.

[19] S. M. Narayan, T. Baykaner, P. Clopton, *et al.*, “Ablation of rotor and focal sources reduces late recurrence of atrial fibrillation compared with trigger ablation alone: Extended follow-up of the CONFIRM trial (conventional ablation for atrial fibrillation with or without focal impulse and rotor modulation),” *Journal of the American College of Cardiology*, vol. 63, no. 17, pp. 1761–1768, May 2014, ISSN: 15583597. DOI: 10.1016/j.jacc.2014.02.543.

[20] K. Shivkumar, K. A. Ellenbogen, J. D. Hummel, J. M. Miller, and J. S. Steinberg, “Acute termination of human atrial fibrillation by identification and catheter ablation of localized rotors and sources: First multicenter experience of focal impulse and rotor modulation (FIRM) ablation,” *Journal of Cardiovascular Electrophysiology*, vol. 23, no. 12, pp. 1277–1285, Dec. 2012, ISSN: 10453873. DOI: 10.1111/jce.12000.

[21] P. M. Boyle, T. Zghaib, S. Zahid, *et al.*, “Computationally guided personalized targeted ablation of persistent atrial fibrillation,” *Nature Biomedical Engineering*, vol. 3, no. 11, pp. 870–879, Nov. 2019, ISSN: 2157846X. DOI: 10.1038/s41551-019-0437-9.

[22] J. J. Rieta, F. Castells, C. Sánchez, V. Zarzoso, and J. Millet, “Atrial activity extraction for atrial fibrillation analysis using blind source separation,” *IEEE Transactions on Biomedical Engineering*, vol. 51, no. 7, pp. 1176–1186, Jul. 2004, ISSN: 00189294. DOI: 10.1109/TBME.2004.827272.

[23] F. Castells, J. Igual, J. J. Rieta, C. Sanchez, and J. Millet, “Atrial fibrillation analysis based on ICA including statistical and temporal source information,” in *ICASSP, IEEE International Conference on Acoustics, Speech and Signal Processing - Proceedings*, vol. 5, Hong Kong, China: IEEE, Apr. 2003, pp. 93–96. DOI: 10.1109/icassp.2003.1199876.

[24] R. J. Martis, U. R. Acharya, and H. Adeli, “Current methods in electrocardiogram characterization,” *Computers in Biology and Medicine*, vol. 48, pp. 133–149, May 2014, ISSN: 00104825. DOI: 10.1016/j.compbiomed.2014.02.012. [Online]. Available: https://linkinghub.elsevier.com/retrieve/pii/S0010482514000432.

[25] S. M. Narayan, D. E. Krummen, K. Shivkumar, P. Clopton, W. J. Rappel, and J. M. Miller, “Treatment of atrial fibrillation by the ablation of localized sources: CONFIRM (Conventional Ablation for Atrial Fibrillation with or Without Focal Impulse and Rotor Modulation) trial,” *Journal of the American College of Cardiology*, vol. 60, no. 7, pp. 628–636, Aug. 2012, ISSN: 07351097. DOI: 10.1016/j.jacc.2012.05.022.

[26] S. M. Narayan, D. E. Krummen, and W. J. Rappel, “Clinical mapping approach to diagnose electrical rotors and focal impulse sources for human atrial fibrillation,” *Journal of Cardiovascular Electrophysiology*, vol. 23, no. 5, pp. 447–454, May 2012, ISSN: 10453873. DOI: 10.1111/j.1540-8167.2012.02332.x.

[27] F. Atienza, J. Almendral, J. Jalife, *et al.*, “Real-time dominant frequency mapping and ablation of dominant frequency sites in atrial fibrillation with left-to-right frequency gradients predicts long-term maintenance of sinus rhythm,” *Heart Rhythm*, vol. 6, no. 1, pp. 33–40, Jan. 2009, ISSN: 15475271. DOI: 10.1016/j.hrthm.2008.10.024.

[28] A. Yaksh, L. J. van der Does, C. Kik, *et al.*, “A novel intra-operative, high-resolution atrial mapping approach,” *Journal of Interventional Cardiac Electrophysiology*, vol. 44, no. 3, pp. 221–225, Dec. 2015, ISSN: 15728595. DOI: 10.1007/s10840-015-0061-x.

[29] M. S. SPACH, R. C. BARR, G. A. SERWER, J. M. KOOTSEY, and E. A. JOHNSON, “Extracellular Potentials Related to Intracellular Action Potentials in the Dog Purkinje System,” *Circulation Research*, vol. 30, no. 5, pp. 505–519, May 1972, ISSN: 0009-7330. DOI: 10.1161/01.RES.30.5.505.

[30] M. Sun, N. M. de Groot, and R. C. Hendriks, “Joint cardiac tissue conductivity and activation time estimation using confirmatory factor analysis,” *Computers in Biology and Medicine*, vol. 144, May 2022, ISSN: 18790534. DOI: 10.1016/j.compbiomed.2022.105393.

[31] A. Alcaine, N. M. De Groot, P. Laguna, J. P. Martínez, and R. P. Houben, “Estimation of high-density activation maps during atrial fibrillation,” in *Computing in Cardiology*, vol. 42, IEEE Computer Society, Feb. 2015, pp. 825–828, ISBN: 9781509006854. DOI: 10.1109/CIC.2015.7411038.

[32] B. Kölling, B. Abdi, N. M. de Groot, and R. C. Hendriks, “Local activation time estimation in atrial electrograms using cross-correlation over higher-order neighbors,” in *European Signal Process-*

*ing Conference*, vol. 2021-January, European Signal Processing Conference, EUSIPCO, Jan. 2021, pp. 905–909, ISBN: 9789082797053. DOI: 10.23919/Eusipco47968.2020.9287434.

[33] C. D. Cantwell, C. H. Roney, F. S. Ng, J. H. Siggers, S. J. Sherwin, and N. S. Peters, "Techniques for automated local activation time annotation and conduction velocity estimation in cardiac mapping," *Computers in Biology and Medicine*, vol. 65, pp. 229–242, Oct. 2015, ISSN: 18790534. DOI: 10.1016/j.compbiomed.2015.04.027.

[34] B. M. Steinhaus, "Estimating cardiac transmembrane activation and recovery times from unipolar and bipolar extracellular electrograms: a simulation study.," *Circulation Research*, vol. 64, no. 3, pp. 449–462, Mar. 1989, ISSN: 0009-7330. DOI: 10.1161/01.RES.64.3.449. [Online]. Available: https://www.ahajournals.org/doi/10.1161/01.RES.64.3.449.

[35] D. H. Johnson and D. E. Dudgeon, *Array Signal Processing: Concepts and Techniques*, 1st ed., A. V. Oppenheim, Ed. Pearson, Feb. 1993, ISBN: 978-0130485137.

[36] H. Krim and M. Viberg, "Two decades of array signal processing research: the parametric approach," *IEEE Signal Processing Magazine*, vol. 13, no. 4, pp. 67–94, Jul. 1996, ISSN: 10535888. DOI: 10.1109/79.526899. [Online]. Available: http://ieeexplore.ieee.org/document/526899/.

[37] S. Saha, S. Hartmann, D. Linz, P. Sanders, and M. Baumert, "A Ventricular Far-field Artefact Filtering Technique for Atrial Electrograms," in *2019 Computing in Cardiology Conference (CinC)*, vol. 45, Computing in Cardiology, Dec. 2019. DOI: 10.22489/cinc.2019.247.

[38] J. Rieta, F. Hornero, R. Alcaraz, and D. Moratal, "Comparison of atrial wave extraction methods from invasive recordings in atrial fibrillation," in *2007 Computers in Cardiology*, vol. 34, IEEE, Sep. 2007, pp. 805–808, ISBN: 978-1-4244-2533-4. DOI: 10.1109/CIC.2007.4745608.

[39] T. Moree, *Estimating atrial activity in epicardial electrograms a beamforming perspective (MSc Thesis)*. Delft, Apr. 2022. [Online]. Available: http://resolver.tudelft.nl/uuid:b00f0e3d-89d1-4327-8b1d-4b7d6076f225.

[40] A.-J. van der Veen and G. Leus, *[COURSE SLIDES] EE4715 Array Processing: 3. Narrowband signals*, 2022.

[41] A. Hyvärinen, J. Karhunen, and E. Oja, *Independent Component Analysis* (Adaptive and Learning Systems for Signal Processing, Communications, and Control). New York, USA: John Wiley & Sons, Inc., May 2001, ISBN: 047140540X. DOI: 10.1002/0471221317.

[42] R. Roy and T. Kailath, "ESPRIT—Estimation of Signal Parameters Via Rotational Invariance Techniques," *IEEE Transactions on Acoustics, Speech, and Signal Processing*, vol. 37, no. 7, pp. 984–995, 1989, ISSN: 00963518. DOI: 10.1109/29.32276.

[43] MathWorks, *k-means clustering*. [Online]. Available: https://nl.mathworks.com/help/stats/kmeans.html.

[44] C. Piech, *K Means*. [Online]. Available: https://stanford.edu/~cpiech/cs221/handouts/kmeans.html.